

Another shipment of six short-period giant planets from *TESS*

Joseph E. Rodriguez¹,^{*} Samuel N. Quinn², Andrew Vanderburg³, George Zhou⁴, Jason D. Eastman², Erica Thygesen¹, Bryson Cale⁵, David R. Ciardi⁵, Phillip A. Reed⁶, Ryan J. Oelkers^{7,8,9}, Karen A. Collins², Allyson Bieryla², David W. Latham², Erica J. Gonzales¹⁰, B. Scott Gaudi¹¹, Coel Hellier¹², Matías I. Jones¹³, Rafael Brahm^{14,15,16}, Kirill Sokolovsky¹, Jack Schulte¹, Gregor Srdoc¹⁷, John Kielkopf¹⁸, Ferran Grau Horta¹⁹, Bob Massey²⁰, Phil Evans²¹, Denise C. Stephens²², Kim K. McLeod²³, Nikita Chazov²⁴, Vadim Krushinsky²⁵, Mourad Ghachoui^{26,27}, Boris S. Safonov²⁸, Cayla M. Dedrick^{29,30}, Dennis Conti³⁰, Didier Laloum³⁰, Steven Giacalone³¹, Carl Ziegler³², Pere Guerra Serra³³, Ramon Naves Noguees³⁴, Felipe Murgas^{35,36}, Edward J. Michaels³⁷, George R. Ricker³, Roland K. Vanderspek³, Sara Seager^{3,38,39}, Joshua N. Winn⁴⁰, Jon M. Jenkins⁴¹, Brett Addison^{42,4}, Owen Alfaro⁴³, D. R. Anderson^{13,44}, Elias Aydi¹, Thomas G. Beatty⁴⁵, Timothy R. Bedding⁴⁶, Alexander A. Belinski²⁷, Zouhair Benkhaldoun²⁵, Perry Berlind², Cullen H. Blake⁴⁷, Michael J. Bowen⁴³, Brendan P. Bowler⁴⁸, Andrew W. Boyle⁵, Dalton Branson⁴⁹, César Briceño⁵⁰, Michael L. Calkins², Emma Campbell²³, Jessie L. Christiansen⁵, Laura Chomiuk¹, Kevin I. Collins⁴³, Matthew A. Cornachione⁵¹, Ahmed Daassou⁵², Courtney D. Dressing³¹, Gilbert A. Esquerdo², Dax L. Feliz⁵³, William Fong³, Akihiko Fukui^{54,35}, Tianjun Gan⁵⁵, Holden Gill³¹, Maria V. Gologuzova²⁷, Jarrod Hansen²², Thomas Henning⁵⁶, Eric G. Hintz¹⁹, Melissa J. Hobson^{56,15}, Jonathan Horner⁴, Chelsea X. Huang⁴, David J. James⁵⁷, Jacob S. Jensen²¹, Samson A. Johnson¹¹, Andrés Jordán^{14,15}, Stephen R. Kane⁵⁸, Khalid Barkaoui^{26,38,35}, Myung-Jin Kim⁵⁹, Kingsley Kim⁶⁰, Rudolf B. Kuhn^{61,62}, Nicholas Law⁶³, Pablo Lewin⁶⁴, Hui-Gen Liu⁶⁵, Michael B. Lund⁵, Andrew W. Mann⁶³, Nate McCrady⁴⁹, Matthew W. Mengel⁴, Jessica Mink², Lauren G. Murphy⁶, Norio Narita^{35,65,66}, Patrick Newman⁴², Jack Okumura⁴, Hugh P. Osborn^{3,67}, Martin Paegert², Enric Palle^{35,36}, Joshua Pepper⁶⁸, Peter Plavchan⁴³, Alexander A. Popov²⁴, Markus Rabus⁶⁹, Jessica Ranshaw¹, Jennifer A. Rodriguez¹, Dong-Goo Roh⁶⁵, Michael A. Reefe³, Arjun B. Savel⁷⁰, Richard P. Schwarz⁷¹, Avi Shporer³, Robert J. Siverd⁷², David H. Sliski⁴⁷, Keivan G. Stassun^{53,73}, Daniel J. Stevens⁷⁴, Abderahmane Soubkiou^{23,75,76}, Eric B. Ting⁴¹, C. G. Tinney⁷⁷, Noah Vowell¹, Payton Walton¹, R. G. West^{44,78}, Maurice L. Wilson², Robert A. Wittenmyer⁴, Justin M. Wittrock⁴³, Shania Wolf⁶⁷, Jason T. Wright^{28,29,79}, Hui Zhang⁸⁰ and Evan Zobel¹

Affiliations are listed at the end of the paper

Accepted 2023 February 7. Received 2023 February 7; in original form 2022 May 11

ABSTRACT

We present the discovery and characterization of six short-period, transiting giant planets from NASA’s *Transiting Exoplanet Survey Satellite (TESS)* – TOI-1811 (TIC 376524552), TOI-2025 (TIC 394050135), TOI-2145 (TIC 88992642), TOI-2152 (TIC 395393265), TOI-2154 (TIC 428787891), and TOI-2497 (TIC 97568467). All six planets orbit bright host stars ($8.9 < G < 11.8$, $7.7 < K < 10.1$). Using a combination of time-series photometric and spectroscopic follow-up observations from the *TESS* Follow-up Observing Program Working Group, we have determined that the planets are Jovian-sized ($R_p = 0.99\text{--}1.45 R_J$), have masses ranging from 0.92 to 5.26 M_J , and orbit F, G, and K stars ($4766 \leq T_{\text{eff}} \leq 7360$ K). We detect a significant

* E-mail: jrod@msu.edu

orbital eccentricity for the three longest-period systems in our sample: TOI-2025 b ($P = 8.872$ d, $0.394^{+0.035}_{-0.038}$), TOI-2145 b ($P = 10.261$ d, $e = 0.208^{+0.034}_{-0.047}$), and TOI-2497 b ($P = 10.656$ d, $e = 0.195^{+0.043}_{-0.040}$). TOI-2145 b and TOI-2497 b both orbit subgiant host stars ($3.8 < \log g < 4.0$), but these planets show no sign of inflation despite very high levels of irradiation. The lack of inflation may be explained by the high mass of the planets; $5.26^{+0.38}_{-0.37} M_J$ (TOI-2145 b) and $4.82 \pm 0.41 M_J$ (TOI-2497 b). These six new discoveries contribute to the larger community effort to use *TESS* to create a magnitude-complete, self-consistent sample of giant planets with well-determined parameters for future detailed studies.

Key words: techniques: radial velocities – techniques: photometric.

1 INTRODUCTION

While NASA’s *Transiting Exoplanet Survey Satellite* (*TESS*) mission continues to discover a wealth of new small planets, it is also discovering many transiting hot and warm Jupiters, complementing the prior work of ground-based transit surveys (Pollacco et al. 2006; Pepper et al. 2007; Bakos et al. 2013) and space-based surveys like NASA’s *Kepler* and *K2* missions (Borucki et al. 2010; Howell et al. 2014) and ESA’s *CoRoT* satellite (Auvergne et al. 2009). These surveys discovered hundreds of hot Jupiters and established that they are rare (< 1 per cent). Using observations from *Kepler*, three different occurrence rates of hot Jupiters have been measured: 0.43 ± 0.05 per cent (Fressin et al. 2013), $0.57^{+0.14}_{-0.12}\%$ (Petigura et al. 2018), and $0.43^{+0.07}_{-0.06}\%$ (Masuda & Winn 2017). However, radial velocity (RV) surveys have measured the occurrence rate to be significantly higher: 1.5 ± 0.6 per cent (Cumming et al. 2008) and 1.2 ± 0.4 per cent (Wright et al. 2012), with the difference in occurrence rates possibly due to the removal of spectroscopic binaries (SB2 that show two sets of lines and short-period single-line spectroscopic binaries (SB1s where only one set of lines is detected but with a large RV offset consistent with a stellar companion) in the RV surveys (Moe & Kratter 2021). Since the surveys have different target selection criteria, these results suggest that the occurrence rates depend on the properties of the host star (mass, multiplicity, age, etc). Zhou et al. (2019) gave a first glimpse into the occurrence rate from the primary mission of NASA’s *TESS* (Ricker et al. 2015)), measuring an occurrence rate of 0.41 ± 0.10 per cent, consistent with results from the *Kepler* mission. Zhou et al. (2019) used *TESS* data to measure occurrence rates as a function of spectral type and found it to be 0.71 ± 0.31 per cent for G stars, 0.43 ± 0.15 per cent for F stars, and 0.26 ± 0.11 per cent for A stars.

As a result of its observing strategy and photometric precision, *TESS* should be nearly complete for discovering transiting hot Jupiters ($P < 10$ days, $TESS_{Mag} < 10$, Zhou et al. 2019), providing the community with the opportunity to create a homogeneous, magnitude-complete population of giant planet parameters. Unfortunately, most ground-based surveys struggled to discover transiting planets with periods above ~ 5 d due to their poor duty cycle (Gaudi, Seager & Mollen-Ornelas 2005). However, much work remains as recent results suggest that the current sample of known hot Jupiters is only 75 per cent complete for stars brighter than *Gaia* magnitude (*Gaia* Collaboration et al. 2018) $G \leq 10.5$, 50 per cent for $G \leq 12$, and 36 per cent at $G \leq 12.5$ (Yee, Winn & Hartman 2021). Fortunately, coordinated RV efforts within the *TESS* Follow-up Observing Program (TFOP) are helping to extend this sample to $G < 12.5$. As we continue to confirm new hot Jupiters from *TESS*, we will gain insight into some of the key questions about their formation and evolutionary pathways (see reviews, e.g. Dawson & Johnson 2018; Fortney, Dawson & Komacek 2021).

Here, we present the discovery and characterization of six new hot and warm giant planets from NASA’s *TESS* mission. These six targets were selected for follow-up confirmation as part of a large effort to discover and characterize transiting hot and warm

Jupiters with the goal of creating a magnitude-complete sample of giant planets with measured eccentricities (Rodríguez et al. 2019, 2021; Ikwut-Ukwa et al. 2022). These discoveries, combined with other large-scale efforts to use *TESS* to confirm and characterize giant planets (Nielsen et al. 2019; Brahm et al. 2020; Addison et al. 2021; Grunblatt et al. 2022, Yee et al. submitted), should lead to a magnitude-complete sample of hot Jupiters for future population studies. During the preparation of this paper, we became aware of another effort to announce the discovery of TOI-2025 b (Knudstrup et al. 2022). Future efforts should combine all observations of TOI-2025 b presented in both discovery papers. All results presented here on TOI-2025 were independently determined, and all communication between both groups was related to coordinating submissions. In §2 we present the *TESS* and follow-up observations. We review our global analysis using EXOFASTv2 (Eastman et al. 2019) in §3 and discuss our results in §4, specifically the impact *TESS* is having on our understanding of hot Jupiters. Our conclusions for this work are summarized in §5.

2 OBSERVATIONS AND ARCHIVAL DATA

We used a series of photometric and spectroscopic observations to rule out false positive scenarios, confirm planet candidates as bona fide planets, and measure key parameters such as orbital eccentricity and the planet’s mass. All observations presented here were coordinated through the TFOP Working Groups. The literature values for previously measured parameters of these stars are listed in Table 1.

2.1 *TESS* photometry

Launched in 2018, NASA’s *TESS* mission has been in full operation with over 200 planets confirmed to date.¹ Using a $24^\circ \times 96^\circ$ field of view, *TESS* monitors each observing sector for ~ 27 d before moving to the next sector (Ricker et al. 2015). During the prime mission, *TESS* observed nearly the entire sky at a 30-min cadence and a pre-selected set of a few hundred thousand stars at 2-min cadence. After a successful 2-yr primary mission that observed each ecliptic hemisphere for about a year, *TESS* began its 27-month first extended mission that is ongoing and has already revisited some of the prime-mission targets but also observed a large portion of the ecliptic plane, where the repurposed *Kepler* mission (*K2*, Howell et al. 2014) discovered over 500 planetary systems and over 1000 more candidates (Barros, Demangeon & Deleuil 2016; Crossfield et al. 2016; Vanderburg et al. 2016; Mayo et al. 2018; Zink et al. 2019; Hardegree-Ullman et al. 2020; Zink et al. 2021, e.g.). During the 27-month extended mission, *TESS* has added a third, 20-s cadence mode for some pre-selected targets and the exposure time of the Full Frame Images (FFI, where the entire $24^\circ \times 96^\circ$ field of view is observed) was reduced to 10 min. To date, *TESS* has announced over 5000 targets

¹<https://exoplanetarchive.ipac.caltech.edu/>

Table 1. Literature and measured properties.

Other identifiers		TOI-1811	TOI-2025	TOI-2145	TOI-2152	TOI-2154	TOI-2497
		TIC 376524552	TIC 394 050 135	TIC 88 992 642	TIC 395 393 265	TIC 428 787 891	TIC 97568 467
		—	—	HIP 86 040	—	—	HD 250 208
TYCHO-2		TYC 1992-00307-1	TYC 4595-00797-1	TYC 3691-00842-1	TYC 4498-01400-1	TYC 4617-00138-1	TYC 0725-01745-1
2MASS		J12354142 + 2712518	J18511077 + 8214436	J17350195 + 4041421	J01452120 + 7747244	J04440676 + 8421511	J06001500 + 1153030
TESS sector		[22]	[14, 18, 19, 20, 24, 25, 26, 40]	[25, 26, 40]	[18, 19, 25, 26]	[19, 20, 25, 26]	[6, 33]
Parameter	Description	Value	Value	Value	Value	Value	Reference
α_{J2000} †	Right ascension (RA)	12:35:41.419	18:51:10.840	17:35:01.950	01:45:21.218	04:44:06.869	06:00:15.008
δ_{J2000} †	Declination (Dec)	+ 27:12:51.923	+ 82:14:43.562	+ 40:41:42.205	+ 77:47:24.623	+ 84:21:51.119	+ 11:53:03.031
G	<i>Gaia</i> G mag.	11.76 ± 0.02	11.36 ± 0.02	8.94 ± 0.02	11.24 ± 0.02	11.04 ± 0.02	9.47 ± 0.02
B _p	<i>Gaia</i> B _p mag.	12.33 ± 0.02	11.69 ± 0.02	9.24 ± 0.02	11.68 ± 0.02	11.32 ± 0.02	9.73 ± 0.02
R _p	<i>Gaia</i> R _p mag.	11.07 ± 0.02	10.90 ± 0.03	8.52 ± 0.02	10.65 ± 0.02	10.61 ± 0.02	9.10 ± 0.02
T	TESS mag.	11.1237 ± 0.0061	10.9461 ± 0.0061	8.5594 ± 0.0063	10.7053 ± 0.0061	10.6611 ± 0.0085	9.1411 ± 0.0063
J	2MASS J mag.	10.280 ± 0.024	10.380 ± 0.025	8.021 ± 0.020	9.973 ± 0.026	10.154 ± 0.025	8.697 ± 0.021
H	2MASS H mag.	9.732 ± 0.027	10.071 ± 0.028	7.810 ± 0.023	9.669 ± 0.030	9.864 ± 0.027	8.533 ± 0.020
K _s	2MASS K _s mag.	9.643 ± 0.025	10.010 ± 0.021	7.761 ± 0.031	9.597 ± 0.024	9.850 ± 0.025	8.486 ± 0.020
WISE1	WISE1 mag.	9.579 ± 0.030	9.995 ± 0.030	7.706 ± 0.030	9.535 ± 0.030	9.808 ± 0.030	8.418 ± 0.030
WISE2	WISE2 mag.	9.668 ± 0.030	10.037 ± 0.030	7.745 ± 0.030	9.543 ± 0.030	9.836 ± 0.030	8.448 ± 0.030
WISE3	WISE3 mag.	9.590 ± 0.042	9.973 ± 0.042	7.717 ± 0.030	9.470 ± 0.032	9.771 ± 0.038	8.424 ± 0.030
WISE4	WISE4 mag.	—	—	7.691 ± 0.122	8.968 ± 0.304	—	8.47 ± 0.365
μ_{α}	<i>Gaia</i> DR2 proper motion in RA (mas yr ⁻¹)	-45.874 ± 0.058	2.791 ± 0.036	-6.512 ± 0.035	27.643 ± 0.040	-10.783 ± 0.036	12.502 ± 0.076
μ_{δ}	<i>Gaia</i> DR2 proper motion in DEC (mas yr ⁻¹)	-10.766 ± 0.035	-4.521 ± 0.045	-3.281 ± 0.040	-11.634 ± 0.048	15.218 ± 0.043	-27.310 ± 0.064
$v \sin i$	Rotational velocity (km s ⁻¹)	3.3 ± 0.5	7.3 ± 0.5	19.4 ± 0.5	5.4 ± 0.5	5.4 ± 0.5	39.6 ± 1.0
π †	<i>Gaia</i> DR2 Parallax (mas)	7.801 ± 0.051	2.978 ± 0.031	4.451 ± 0.031	3.302 ± 0.042	3.374 ± 0.034	3.507 ± 0.051

Notes. The uncertainties of the photometry have a systematic error floor applied.

† RA and Dec are in epoch J2000. The coordinates come from Vizier where the *Gaia* RA and Dec have been preprocessed and corrected to J2000 from epoch J2015.5.

‡ Values have been corrected for the -0.30 μ s offset as reported by Lindgren et al. (2018) but this is not significant for these systems.

References are: ¹ Gaia Collaboration et al. (2018), ² Staassun et al. (2018), ³ Curri et al. (2003), ⁴ Curri et al. (2010)

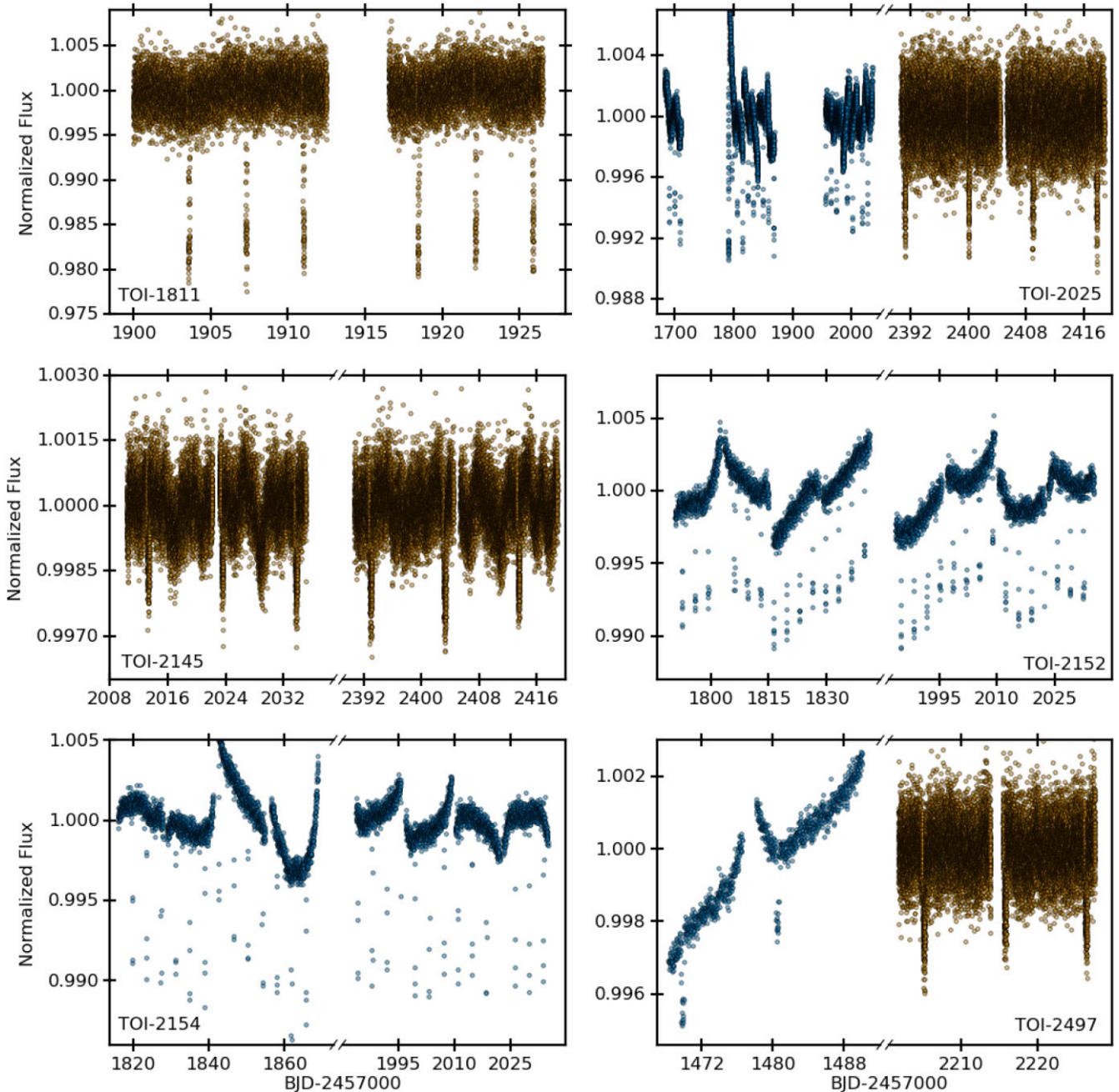


Figure 1. The *TESS* 30-min light curves extracted using the technique described in Section 2.1 (blue) and 2-min SPOC light curves (orange) for TOI-1811 (top-left), TOI-2025 (top-right), TOI-2145 (middle-left), TOI-2152 (middle-right), TOI-2154 (bottom-left), and TOI-2497 (bottom-right).

that display a signal consistent with it being an exoplanet, which are known as *TESS* Objects of Interest.² (TOIs, Guerrero et al. 2021), targets that display a signal consistent with it being an exoplanet.

TESS observed all six TOIs presented here during the 2-yr primary mission, and, in the cases of TOI-2025 and TOI-2497, reobserved during the extended mission. TOI-1811 and TOI-2145 were only observed at 2-min cadence, TOI-2152 and TOI-2154 were only observed in the 30-min full frame images, and TOI-2025 and TOI-2497 were observed in both cadences during different sectors (see Fig. 1). For the 2-min observations, the *TESS* images were downlinked,

reduced, and analyzed by the Science Processing Operations Center (SPOC) pipeline (Smith et al. 2012; Stumpe et al. 2014; Jenkins et al. 2016). The final SPOC lightcurves were searched for transits with the SPOC Transiting Planet Search (TPS, Jenkins 2002). The final processed lightcurves were downloaded from the Mikulski Archive for Space Telescopes (MAST) archive and included in our global fitting (see Section 3).

For our final transit fits, we adopt the SPOC 2-min lightcurves when available but we re-extracted the 30-min FFI light curves using a custom full frame image pipeline derived from that of Vanderburg et al. (2019). We downloaded the pixels surrounding the locations of each host star using the *TESS*Cut interface (Brasseur et al. 2019) to the MAST. We first extracted light curves from a series of 20 different

²<https://tess.mit.edu/toi-releases/>

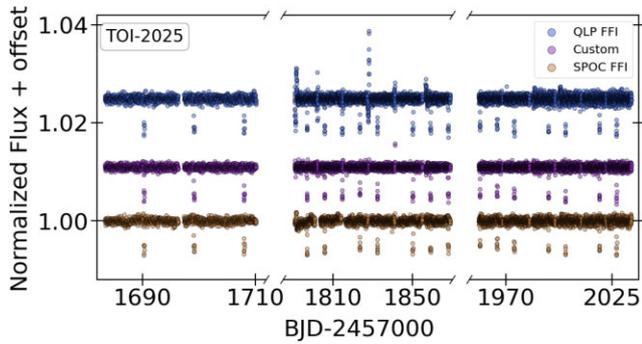


Figure 2. The flattened *TESS* 30-min light curves reduced using with the Quick Look Pipeline (Blue, Huang et al. 2020), Custom (purple, Vanderburg et al. 2019), and flattened *TESS*-SPOC light curves generated from the FFIs (Orange, Jenkins et al. 2016; Caldwell et al. 2020) for TOI-2025. These lightcurves are flattened using *Keplerspline* (as described in Section 2.1) prior to being included in the global fit (see Section 3).

photometric apertures. We then removed systematic errors from each light curve by decorrelating with the mean and standard deviations of the spacecraft quaternion time series within each exposure and the *TESS* SPOC pipeline’s Presearch Data Condition (PDC) cotrending basis vectors (binned to the cadence of each sector’s observations). We performed the decorrelation via linear regression, where we solved for the best-fit coefficients for each model component using a matrix inversion technique, while iteratively excluding outlier points. We also included a basis spline in our linear regression model to simultaneously account for the stars’ photometric variability. After subtracting the best-fit systematics components from our linear regression from the light curve, we then applied a correction for dilution from nearby stars customized for each of the 20 apertures based on a model of the *TESS* pixel response function and the known positions and magnitudes from the *TESS* Input Catalog (TIC, Stassun et al. 2018) of nearby stars. Finally, for each star we selected one of the 20 photometric apertures by finding which one minimized its photometric scatter (outside of transit) and chose that as the final light curve for each star. We compared our final FFI lightcurve of TOI-2025 with that created by the SPOC pipeline and the MIT Quick Look Pipeline (QLP, Huang et al. 2020) as a check for the lightcurve quality (see Fig. 2). We adopt our custom FFI lightcurve for the final global fitting but note no significant difference in the transit properties when comparing the three versions of the FFI lightcurves. Additionally, we have photometric follow-up transits from the ground for each system other than TOI-2497.

To properly fit our *TESS* photometry within the global fit, we flatten the out-of-transit features using *Keplerspline*³, which fits a spline to the variability seen and divides out the best-fit model (Vanderburg & Johnson 2014). The spline requires spacing for the break points (breaks in the spline to handle discontinuities) and we optimized this by following the methodology from Shallue & Vanderburg (2018) to minimize the Bayesian information criterion. Most of the out-of-transit information provides little to no useful information in determining the full system parameters in the case of these six TOIs but is still computationally intensive to model. Therefore, we remove all baseline photometry from the *TESS* lightcurves, only keeping one full transit duration before the transit until one full transit duration after each transit. In the global model, we modeled all flattened

lightcurve segments for each system of a given cadence with the same zero point and added variance (see Section 3).

2.2 Kilodegree extremely little telescope photometry

Since *TESS* focuses on observing bright ($V < 12$) stars, there is a wealth of archival data on these targets from even small-aperture surveys like the Kilodegree Extremely Little Telescope (KELT) survey⁴ (Pepper et al. 2007, 2012; Pepper, Stassun & Gaudi 2018). See Siverd et al. (2012) & Kuhn et al. (2016) for a discussion on the KELT-North and KELT-South observing strategy and reduction techniques. KELT uses two small aperture telescopes (Mamiya 645 80 mm f/1.9 lens with 42 mm aperture, Apogee 4k×4k CCD) to observe most of the entire sky on a 20–30 min cadence. Light curves from the KELT survey are accessible through the NASA Exoplanet Archive⁵

We do not recover the transits detected by *TESS*, likely due to a combination of the poor duty cycle from the ground (for the longer period systems, Gaudi et al. 2005), the faintness of the host stars (for the shorter orbital period systems), and some of the transits being shallow (< 0.5 per cent). However, KELT data can be useful to measure stellar rotation periods. Following the approach of Stassun et al. (1999); Oelkers et al. (2018); Rodriguez et al. (2021), we executed a search for periodic signals using the KELT data. For these stars, we post-processed the light curve data using the Trend-Filtering Algorithm (Kovács, Bakos & Noyes 2005) to remove common systematics. We then searched for candidate rotation signals using a modified version of the Lomb–Scargle period finder algorithm (Lomb 1976; Scargle 1982). We searched for periods between a minimum period of 0.1 d and a maximum period of 100 days using the autopower feature of the *astropy* implementation of Lomb–Scargle. We masked periods between 0.5 and 0.505 d and 0.97–1.04 d to avoid the most common detector aliases associated with KELT’s observational cadence and its interaction with the periods for the solar and sidereal day. For each star, we selected the highest statistically significant peak of the power spectrum as the candidate period for stellar variability.

We then executed a boot-strap analysis, using 100 Monte-Carlo iterations, where the dates of the observations were not changed but the magnitude values of the light curve were randomized, following the work of Henderson & Stassun (2012); VanderPlas (2018). We recalculated the Lomb–Scargle power spectrum for each iteration, and recorded the maximum peak power of all iterations. If the highest power spectrum peak was larger than the maximum simulated peak after 100 iterations, then we considered the periodic signal to be a candidate rotation period. We find only TOI-1811 to have a significant candidate rotation period at 25.779 d using KELT data.

2.3 Wide angle survey for planets photometry

Additional observations were available for only TOI-1811 from the Wide Angle Survey for Planets (WASP) survey. Each WASP site (La Palma and SAAO) used an array of eight 200-mm, f/1.8 lenses to create a large field of view (Pollacco et al. 2006). The typical cadence of the observations were 15–30 min. Observations of TOI-1811 from 2007 and 2011 were available and following the techniques from Maxted et al. (2011), we searched for periodic modulation consistent with the rotation period of the star. We find a similar period to that

⁴<https://keltsurvey.org>

⁵<https://exoplanetarchive.ipac.caltech.edu/cgi-bin/TblSearch/nph-tblSearch.html?app=ExoTbls&config=kelttimeseries>

³<https://github.com/avanderburg/keplerspline>

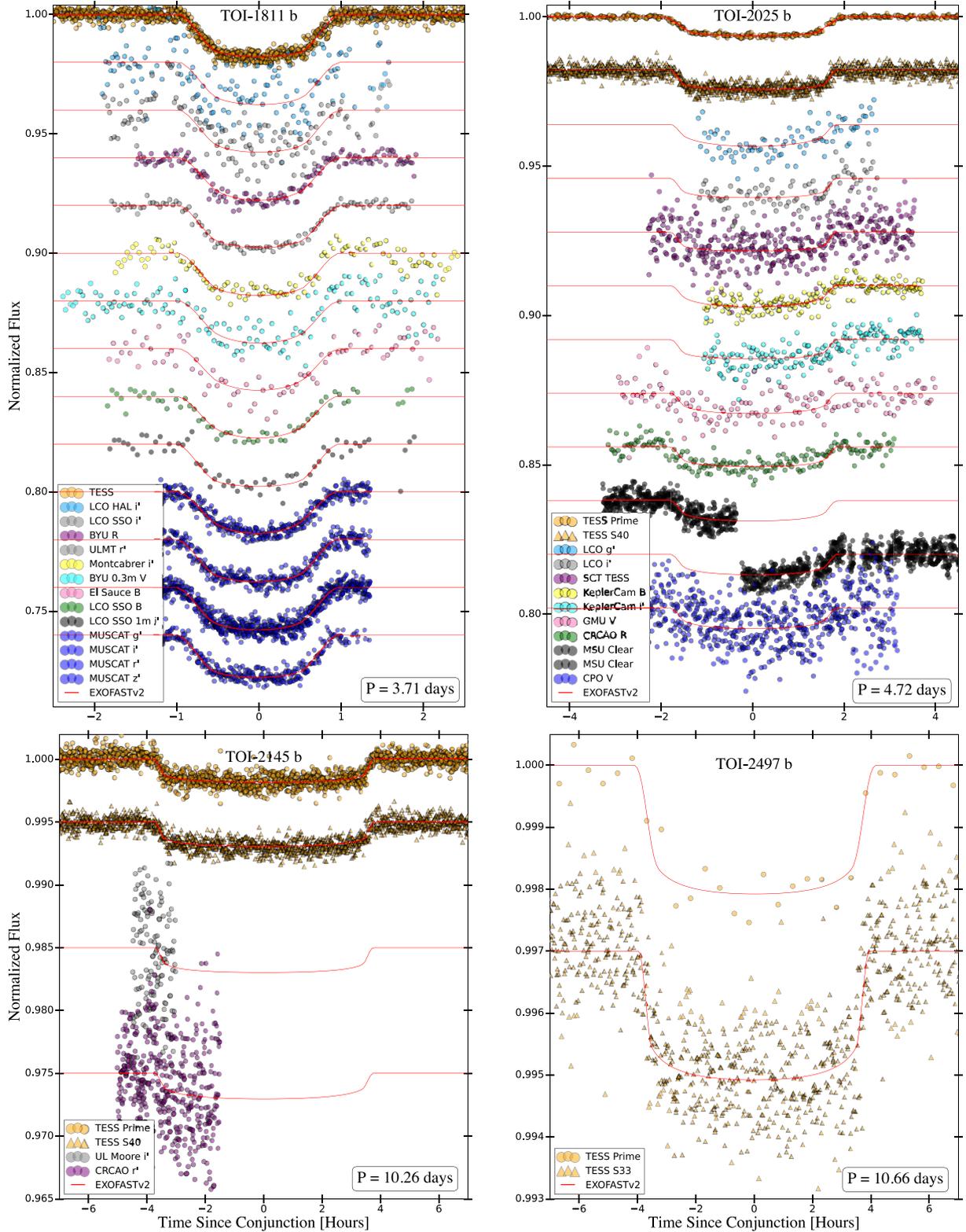


Figure 3. The *TESS* (orange) and TFOF SG1 follow-up transits of TOI-1811 b (top-left), TOI-2025 b (top-right), TOI-2145 b (bottom-left), and TOI-2497 b (bottom-right). The EXOFASTv2 model for each transit observation is shown by the red solid line.

what was in the KELT data, 23 ± 1 days. Additionally, using the WASP search algorithm described in Collier Cameron et al. (2007) on the observations and the identification of planetary period of TOI-1811 b from *TESS*, we measure the WASP ephemeris of planet to

be a period of 3.7130803 ± 0.0000292 and a mid-transit epoch (T_C) of $2454006.04900 \pm 0.00337$ HJD_{TDB}. This ephemeris is consistent with the *TESS* ephemeris and therefore is used as a prior for the EXOFASTv2 global analysis of TOI-1811 b (see Section 3).

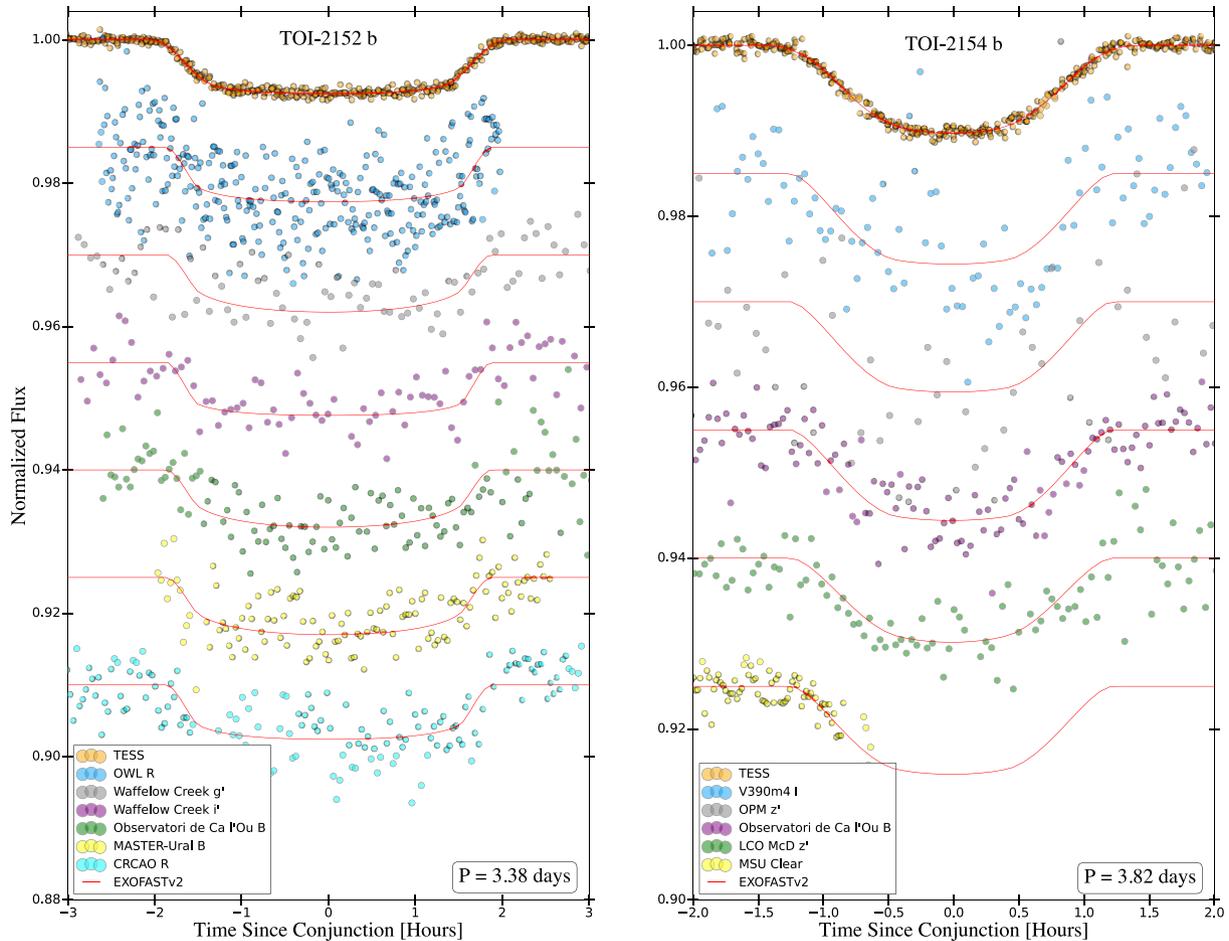


Figure 4. The *TESS* (orange) and TFOP SG1 follow-up transits of TOI-2152A b (left) and TOI-2154 b (right). The EXOFASTv2 model for each transit observation is shown by the red solid line.

2.4 Ground-based photometry from the *TESS* follow-up observing program working group

As part of the confirmation processes within TFOP, we observed five of the six giant planet systems presented in this paper using a variety of small-aperture (< 2 m) telescopes to confirm the transit was on target and to refine the system parameters (particularly increasing the photometric baseline to improve our precision and accuracy on future times of transit). Observations were obtained using the Las Cumbres Observatory (LCO) telescope network (Brown et al. 2013), KeplerCam on the 1.2m telescope at Fred Lawrence Whipple Observatory (FLWO), C. R. Chambliss Astronomical Observatory (CRCAO) at Kutztown University, Brigham Young University’s campus telescopes, El Sauce Observatory, MUSCAT2 on the 1.5 m Telescopio Carlos Sánchez (TCS), the University of Louisville’s Moore Observatory, Michigan State University’s Observatory, George Mason University’s Observatory, Optical Wide-field patrol network (OWL-Net) Oukaimeden observatory (OWL), Waffelow Creek Observatory, Observatori de Ca l’Ou, MASTER-Ural observatory, Villa’39 Observatory, Observatoire Privé du Mont (OPM), Conti Private Observatory (CPO), and Kotizarovci Observatory. Table 2 shows the information on each observatory and the detrending parameters used within the global fit. The photometric observations were reduced and aperture photometry extraction was conducted using *AstroImageJ* (Collins et al. 2017) for all follow-

up transit observations except MUSCAT2 and the MASTER-Ural observations. Below we briefly review the reduction process used for these facilities. Unfortunately, due to its longer orbital period, we were not able to get photometric follow-up on TOI-2497.

Two of our follow-up transit observations did not use *AstroImageJ* to perform the reduction and photometry. TOI-1811 was observed on the night of UT 2021 June 05 with the multicolor imager *MUSCAT2* (Narita et al. 2019) mounted on the 1.5 m Telescopio Carlos Sánchez (TCS) at Teide Observatory, Spain. The raw data were reduced by the *MUSCAT2* pipeline (Parviainen et al. 2019) which performed a standard image calibration and aperture photometry. TOI-2152 was observed on UT 2020 December 12 with MASTER-Ural 0.4 m telescope. The data reduction included standard dark, flat field and astrometry corrections, and is performed using the MASTER-Ural pipeline.⁶ Comparison stars were selected from the *Gaia* DR2 catalog. Aperture photometry of the object and the ensemble of comparison stars was performed using Python/Photutils (Bradley et al. 2019). Photometric data processing and detrending was completed with the Python version of the *Astrokit* (Burdanov, Krushinsky & Popov 2014), to minimize the standard deviation of the ensemble of comparison stars.

⁶<https://master.kourovka.ru/>

Table 2. Photometric follow-up observations of these systems used in the global fits and the detrending parameters.

Target	Observatory	Date (UT)	size (m)	Filter	FOV	Pixel scale	Exp (s)	Additive detrending
TOI-1811 b	LCO SSO	2020 April 23	0.4	<i>i'</i>	19' × 29'	0.57"	55	Airmass
TOI-1811 b	LCO HAL	2020 April 23	0.4	<i>i'</i>	19' × 29'	0.57"	55	Airmass
TOI-1811 b	BYU	2020 April 27	0.6	<i>R</i>	32' × 32'	0.93"	70	Airmass
TOI-1811 b	ULMT	2020 April 27	0.6	<i>i'</i>	26.8' × 26.8'	0.395"	128	Airmass
TOI-1811 b	Montcabrer	2020 April 27	0.3	<i>i'</i>	45.8' × 45.8'	0.9"	120	Airmass
TOI-1811 b	BYU-12	2020 May 08	0.6	<i>V</i>	25' × 19'	0.92"	90	Airmass
TOI-1811 b	El Sauce	2020 May 12	0.36	<i>B</i>	19' × 13'	1.47"	180	Airmass
TOI-1811 b	LCO SSO	2021 February 25	1.0	<i>z'</i>	27' × 27'	0.39"	55	Airmass
TOI-1811 b	LCO SSO	2021 February 25	1.0	<i>B</i>	27' × 27'	0.39"	70	Airmass
TOI-1811 b	MUSCAT2	2021 June 05	1.52	<i>g'</i>	7.4' × 7.4'	0.44"	30	Airmass
TOI-1811 b	MUSCAT2	2021 June 05	1.52	<i>i'</i>	7.4' × 7.4'	0.44"	30	Airmass
TOI-1811 b	MUSCAT2	2021 June 05	1.52	<i>r'</i>	7.4' × 7.4'	0.44"	15	Airmass
TOI-1811 b	MUSCAT2	2021 June 05	1.52	<i>z'</i>	7.4' × 7.4'	0.44"	30	Airmass
TOI-2025 b	Kotizarovci	2020 June 26	0.3	<i>TESS</i>	15' × 23'	1.2064"	30	Airmass
TOI-2025 b	LCO TFN	2020 June 26	0.4	<i>g'</i>	19' × 29'	0.57"	60	Airmass
TOI-2025 b	FLWO/KeplerCam	2021 May 12	1.2	<i>B</i>	23.1' × 23.1'	0.672"	20	Airmass
TOI-2025 b	FLWO/KeplerCam	2021 May 12	1.2	<i>i'</i>	23.1' × 23.1'	0.672"	7	Airmass
TOI-2025 b	GMU	2021 May 21	0.8	<i>R</i>	23' × 23'	0.34"	50	Airmass
TOI-2025 b	CRCAO	2021 May 21	0.61	<i>R</i>	19.5' × 13'	0.39"	120	Airmass
TOI-2025 b	MSU	2021 September 30	0.61	<i>Clear</i>	9.5' × 9.5'	0.55"	20	None
TOI-2025 b	MSU	2021 October 18	0.61	<i>Clear</i>	9.5' × 9.5'	0.55"	30	None
TOI-2025 b	CPO	2021 December 29	0.61	<i>V</i>	23' × 18'	1"	30	Total counts
TOI-2145 b	CRCAO	2021 Sept 07	0.61	<i>r'</i>	19.5' × 13'	0.39"	20	Airmass
TOI-2145 b	Moore	2021 Sept 07	0.61	<i>i'</i>	26.8' × 26.8'	0.39"	20	Airmass
TOI-2152 b	OWL	2020 August 17	0.5	<i>B</i>	1.1° × 1.1°	1"	20	Airmass
TOI-2152 b	Waffelow Creek	2020 October 11	0.36	<i>g'</i>	27' × 15'	0.66"	90	Airmass
TOI-2152 b	Waffelow Creek	2020 October 11	0.36	<i>i'</i>	27' × 15'	0.66"	90	Airmass
TOI-2152 b	Observatori de Ca l'Ou	2020 November 24	0.4	<i>B</i>	19' × 19'	1.14"	150	Airmass
TOI-2152 b	MASTER-Ural	2020 December 12	0.4	<i>R</i>	2° × 2°	1.85"	80	Airmass
TOI-2152 b	CRCAO	2021 June 28	0.61	<i>R</i>	19.5' × 13'	0.39"	120	Airmass
TOI-2154 b	V39-0m4	2020 August 18	0.4	<i>I</i>	32' × 32'	0.95"	60	Airmass
TOI-2154 b	OPM	2020 October 29	0.2	<i>z'</i>	39' × 29'	0.69"	180	Airmass
TOI-2154 b	Observatori de Ca l'Ou	2020 November 23	0.4	<i>B</i>	19' × 19'	1.14"	110	Airmass
TOI-2154 b	LCO McDonald	2020 December 03	1.0	<i>z'</i>	27' × 27'	0.39"	45	Airmass
TOI-2154 b	MSU	2021 October 24	0.61	<i>Clear</i>	9.5' × 9.5'	0.55"	60	Airmass
TOI-2497 b	None							

Note. All the follow-up photometry presented in this paper is available in machine-readable form in the online journal. See §D in the appendix of Collins et al. (2017) for a description of each detrending parameter.

2.5 Spectroscopy

To confirm these six systems as bona fide transiting giant planets by removing any remaining false positive scenario, we obtained time-series spectroscopic measurements of each target coordinated through TFOP. These RV measurements, combined with the transit photometry, allowed us to precisely measure the mass and orbital eccentricity of each system, a key component in understanding their evolutionary origins. Table 3 shows a sample RV point per target per instrument (the full table will be available in machine-readable form in the online journal). The RVs and best-fit models from our EXOFASTv2 analysis are shown in Fig. 5 (see Section 3).

2.5.1 Tillinghast reflector echelle spectrograph spectroscopy

Using the Tillinghast Reflector Echelle Spectrograph (TRES; Fűrész 2008)⁷ on the 1.5m Tillinghast Reflector, we measured the radial velocity orbit of all six TOIs presented in this paper. The telescope

Table 3. One RV point from each spectrograph for all six systems. The full table of RVs for each system is available in machine-readable form in the online journal.

BJD _{TDB}	RV (m s ⁻¹)	σ_{RV}^\dagger (m s ⁻¹)	Target	Instrument
2459206.966936	-91.2	24.7	TOI-1811	TRES
2459060.767111	395.0	39.8	TOI-2025	TRES
2459097.65584	-194.7	103.1	TOI-2145	MINERVA T1
2459326.76336	311.8	51.8	TOI-2145	MINERVA T2
2459330.93081	94.6	167.0	TOI-2145	MINERVA T3
2459072.693111	70.6	60.6	TOI-2145	TRES
2459095.870551	481.26	40.01	TOI-2152	TRES
2459201.888606	90.4	43.7	TOI-2154	TRES
2459596.60687	385.0	76.0	TOI-2497	CHIRON
2459279.908926	56275.1	271.6	TOI-2497	M-Australis T3
2459504.223682	56250.9	316.1	TOI-2497	M-Australis T4
2459279.908926	56019.7	340.9	TOI-2497	M-Australis T6
2459271.812986	-634.1	71.0	TOI-2497	TRES

Note. [†] The internal RV error for the observation shown.

⁷<http://www.sao.arizona.edu/html/FLWO/60/TRES/GABORthesis.pdf>

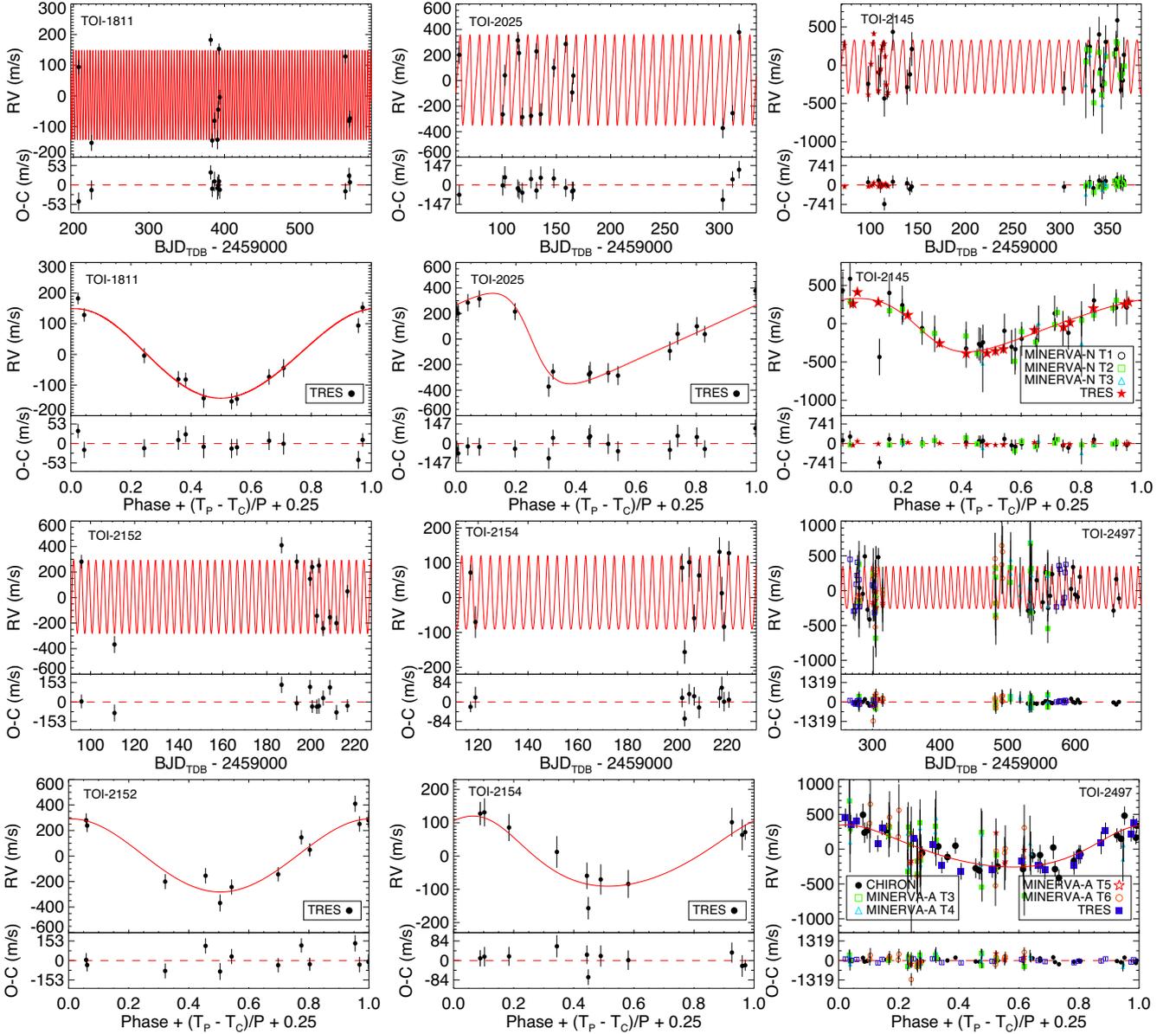


Figure 5. The RV observations of TOI-1811 (top-left), TOI-2025 (top-middle), TOI-2145 (top-right), TOI-2152 (bottom-left), TOI-2154 (bottom-middle), and TOI-2497 (bottom-right). In each case, the top figure shows the RVs versus time and the bottom panel is phased to the best-fit ephemeris from our global fit. The EXOFASTv2 model is shown in red and the residuals to the best-fit are shown below each plot.

and spectrograph are located at the Fred L. Whipple Observatory (FLWO) on Mt. Hopkins, AZ. The reduction and RV analysis followed the procedure described in Buchhave et al. (2010) and Quinn et al. (2012). The only difference is that the template spectra for the RV extraction were created by median-combining all of the out-of-transit spectra (after shifting each to align them). To rule out scenarios in which the apparent velocity variation is caused by a blended binary or stellar activity, we performed a line bisector analysis on the TRES spectra following the work of Torres et al. (2007). In all six cases, we find no evidence for these false positive scenarios in the bisector span variations. The bisector span measurements do not correlate with the derived radial velocities or orbital phase, and the measurements for each star agree to within the uncertainties. The TRES spectra were also analyzed using the Stellar Parameter Classification (SPC) package (Buchhave et al. 2012) to determine the $[\text{Fe}/\text{H}]$, T_{eff} , and rotational velocity of each host star (see Tables 1 and 6).

2.5.2 CHIRON spectroscopy

We obtained 26 spectra of TOI-2497, between UT 2021 March 06 and UT 2022 March 25. The data were taken with the CHIRON (Tokovinin et al. 2013) high-resolution spectrograph, installed in the 1.5 m telescope at the Cerro Tololo International Observatory. The observations were performed with the image slicer ($R \sim 80000$), with exposure times between 600s and 1800s, leading to a SNR per extracted pixel between ~ 20 – 80 , at 550 nm. For each observation, we obtained a ThAr spectrum immediately before the science spectra to account for the instrument spectral drift, and thus a new wavelength solution was automatically computed from that calibration, by the CHIRON pipeline (Paredes et al. 2021). The radial velocities were computed using an updated version of the pipeline used in Jones et al. (2019). A sample of the resulting values are listed in Table 3.

2.5.3 *Minerva-Australis spectroscopy*

We make use of the Minerva-Australis array for additional radial velocities of TOI-2497. Minerva-Australis is an array of four identical 0.7 m telescopes located at Mt Kent Observatory, Australia. The telescopes are fed by four independent fibers into the KiwiSpec high resolution échelle spectrograph, yielding a spectral resolving power of $R \sim 80\,000$ over the wavelength range of 5000–6300 Å (Addison et al. 2019). Simultaneous wavelength calibration is provided by two calibration fibers, illuminated by a quartz lamp through an iodine cell, that tracks the instrument drift over an exposure. Radial velocities are measured from each telescope independently via a least-squares deconvolution between the extracted spectra and a synthetic, following the procedure described in Zhou et al. (2021). The template is generated from an ATLAS9 atmosphere model (Castelli & Hubrig 2004) at the atmosphere parameters of the target star, and has no rotational broadening applied. The resulting line-broadening function is modeled with a kernel describing the rotational, macroturbulent, and instrumental broadening effects, as well as the radial velocity shift of a given exposure.

2.5.4 *MINERVA north spectroscopy*

The MINERVA North observations of TOI-2145 were made with the MINERVA telescope array and KiwiSpec Spectrograph (Swift et al. 2015; Wilson et al. 2019), which consists of four robotic telescopes at Whipple Observatory in Arizona, fiber fed to a temperature and pressure stabilized, $R \sim 80\,000$, iodine cell calibrated spectrograph. We obtained 24 observations with T1, 16 observations with T2, and 5 observations with T3 spanning from UT 2020 May 09 to UT 2021 May 31. We extracted one-dimensional (1D) spectra from the two-dimensional (2D) spectra with our standard methods.

The corresponding MINERVA RVs are computed from the 1D spectra with `pychell` using updated methods compared to those described in Cale et al. (2019). Each 1D spectrum is forward modeled on a per-order basis. The model accounts for the wavelength solution, instrumental profile (IP), continuum, tellurics, and stellar Doppler shift. An iodine vapor gas cell in the calibration unit constrains the wavelength solution and IP. We use the Fourier Transform Spectrometer (FTS) scan measured at NIST, described in Wilson et al. (2019). A synthetic BT-Settl model ($T_{\text{eff}} = 6000$ K, $\log g = 3.5$, $(Fe/H)_{\odot} = 0$) is used as an initial stellar template, which is further Doppler broadened to $v \sin i = 19$ km s⁻¹ with PyAstronomy (Czesla et al. 2019). `pychell` then iteratively updates this template based on the residuals between the data and model, and although the fits suggest the stellar template is more accurate at later iterations, the corresponding RVs are inconsistent with the orbit of the planet, whereas the initial BT-Settl template yields consistent RVs with the TRES observations which strongly support the planetary orbit. To ensure that the MINERVA North observations were not improperly influencing our results, we ran a global fit using only the TRES RVs and the results were consistent to 1σ . We have yet to find cause for the loss of accuracy at later iterations, and is a subject of future work. We therefore use RVs from the first iteration. The RMS of the residuals of our adopted RV model suggest a median S/N per-spectral pixel of 17.

2.6 High-resolution imaging

As part of our standard process for validating transiting exoplanets to assess the possible contamination of bound or unbound companions on the derived planetary radii (Ciardi et al. 2015), we observed the TOIs with a combination of high-resolution imaging resources

including near-infrared adaptive optics (AO) imaging at Lick (TOI-2145, TOI-2497) and Palomar (TOI-1811, TOI-2145) Observatories and with optical speckle imaging using the 2.5m SAI telescope (TOI-1811, TOI-2025, TOI-2145, TOI-2152, TOI-2154) and the Southern Astrophysical Research (SOAR) telescope (TOI-2497). While the optical speckle observations tend to provide higher resolution, the NIR AO observations tend to provide better sensitivity, especially to lower-mass stars. If a companion is detected, the combination of the observations in multiple filters enables better characterization. Additionally, recent studies have shown that *Gaia* (DR2 and eDR3) (Gaia Collaboration et al. 2018) is most efficient at identifying companions with separations greater than ~ 0.5 –1 arcsec (Ziegler et al. 2018). *Gaia* eDR3 (Gaia Collaboration et al. 2021) is also used to identify targets that have a large Renormalized Unit Weight Error (RUWE) value indicative of a poor astrometric fit assuming a single-star model and possibly indicating the presence of undetected stellar companions. For all of the observations, we only detect one faint companion to TOI-2152 ($\Delta\text{Mag} \sim 5$) within 1 arcsec of the primary target.

2.6.1 *Summary of adaptive optics (AO) observations*

The Palomar Observatory observations of TOI-1811 and TOI-2145 were made with the PHARO instrument (Hayward et al. 2001) behind the natural guide star adaptive optics (AO) system P3K (Dekany et al. 2013) on UT 2021 February 23 and UT 2021 February 24, respectively, in a standard five-point quincunx dither pattern with steps of 5 arcsec in the narrow-band $Br - \gamma$ filter ($\lambda_0 = 2.1686$; $\Delta\lambda = 0.0326$ μm). Each dither position was observed three times, offset in position from each other by 0.5 arcsec for a total of 15 frames; with an integration time of 30 and 1.4 seconds per frame, respectively for total on-source times of 450 and 21 s. PHARO has a pixel scale of 0.025 arcsec per pixel for a total field of view of ~ 25 arcsec.

We also observed TIC 88 992 642 (TOI-2145) and TIC 97 568 467 (TOI-2497) on UT 2021 March 29 using the ShARCS camera on the Shane 3-m telescope at Lick Observatory (Kupke et al. 2012; Gavel et al. 2014; McGurk et al. 2014). Observations were taken with the Shane adaptive optics system in natural guide star mode in order to search for nearby, unresolved stellar companions. For each target, we collected sequences of observations using a K_s filter ($\lambda_0 = 2.150$ μm , $\Delta\lambda = 0.320$ μm) and a J filter ($\lambda_0 = 1.238$ μm , $\Delta\lambda = 0.271$ μm). We reduced the data using the publicly available `SIMMER` pipeline (Savel et al. 2020).⁸ We find no nearby stellar companions within our detection limits.

The AO data were processed and analyzed with a custom set of IDL tools. The science frames were flat-fielded and sky-subtracted. The flat fields were generated from a median average of dark subtracted flats taken on-sky. The flats were normalized such that the median value of the flats is unity. The sky frames were generated from the median average of the 15 dithered science frames; each science image was then sky-subtracted and flat-fielded. The reduced science frames were combined into a single combined image using an intra-pixel interpolation that conserves flux, shifts the individual dithered frames by the appropriate fractional pixels, and median-coadds the frames. The final resolutions of the combined dithers were determined from the FWHM of the point spread functions for each of the stars: 0.102 arcsec for TOI-1811 and 0.092 arcsec for TOI-2145. The sensitivities of the final combined AO image were determined by injecting simulated sources azimuthally around the primary target every 20° at separations of integer multiples of the central source’s FWHM (Furlan et al. 2017). The brightness of each injected source

⁸<https://github.com/arjunsavel/SIMMER>

Table 4. Binariness parameters of TOI-2152B on the basis of SPP observations: separation, position angle, and magnitude difference in *I* band.

Date (UT)	ρ''	P.A. $^\circ$	Δm
2020 Oct 21	0.765 ± 0.008	85.2 ± 0.2	4.8 ± 0.2
2020 Oct 28	0.762 ± 0.009	86.1 ± 0.3	4.8 ± 0.1
2020 Dec 02	0.770 ± 0.008	87.0 ± 0.2	4.8 ± 0.1
2021 Jul 17	0.782 ± 0.008	85.8 ± 0.2	4.6 ± 0.1

Note. The ρ'' is the projected separation of the neighbor, if at the distance of the primary star.

was scaled until standard aperture photometry detected it with 5σ significance. The resulting brightness of the injected sources relative to primary target set the contrast limits at that injection location. The final 5σ limit at each separation was determined from the average of limits at that separation (across all azimuthal samples) and the uncertainty on the limit was set by the rms dispersion of the azimuthal slices at a given radial distance. For both TOI-1811 and TO-2145, no additional stellar companions were detected in agreement with the other observations. All high-spatial resolution observations are available publicly on Exofop⁹.

2.6.2 Speckle imaging

Using the 4.1-m SOAR telescope, we obtained speckle imaging of TOI-2497 using HR Cam on UT 2021 February 27 in the *I*-band following the observing and reduction strategy described in Tokovinin (2018). HRCam on SOAR has a 15 arcsec \times 15 arcsec field of view and had a 0.01575 arcsec pixel scale. With a contrast of ΔMag of 7.7 at 1 arcsec, we detected no nearby companions around TOI-2497. For a complete description of the observing strategy for *TESS* targets, see Ziegler et al. (2020).

TOI-1811, TOI-2025, TOI-2145, TOI-2152, and TOI-2154 were observed with the Speckle Polarimeter (Safonov, Lysenko & Dodin 2017) on the 2.5 m telescope at the Caucasian Observatory of Sternberg Astronomical Institute (SAI) of Lomonosov Moscow State University. SPP uses Electron Multiplying CCD Andor iXon 897 as a detector. The atmospheric dispersion compensator allowed observation of relatively faint targets through the wide-band I_c filter. For TOI-2145 we used a medium band interference filter with FWHM of 50 nm and centered on 625 nm. The power spectrum was estimated from 4000 frames with 30 ms exposure. The detector has a pixel scale of 20.6 mas pixel⁻¹. For all targets except for TOI-2152 we did not detect stellar companions, the contrast limits at 1 arcsec are $\Delta \text{mag} = 6.7$ (TOI-1811), 6.4 (TOI-2025), 3.3 (TOI-2145), 5.9 (TOI-2152), this had multiple observations ranging from 4.7 to 6.3), and 6.5 (TOI-2154). We note that the difference image analysis performed in the data validation reports from *TESS* show that the source of the transit signal for TOI-2145 was located within 5.0 ± 2.7 arcsec and for

⁹<https://exofop.ipac.caltech.edu/tess/>

TOI-1811 was within 1.78 ± 2.5 arcsec, complementing the high resolution imaging results.

TOI-2152 is the only star that we found to have a close-in stellar companion. The separation, position, and contrast of the TOI-2152 inner companion were estimated on 4 dates; the results are presented in Table 4. According to proper motion from *Gaia* eDR3, the primary star is expected to move by 22 ± 0.02 mas over the period of our observations, from UT 2020 October 21 to UT 2021 July 17; however, there apparent motion is only 13 ± 11 mas which is consistent with no discernible separation change. While not definitive, the companion appears to be a common proper motion companion and is likely gravitationally bound. With a contrast of $\Delta I = 4.8$ mag, the detection is consistent with the companion being an M1V star ($(M \sim 0.5M_\odot; T_{\text{eff}} \sim 3600\text{K}; \text{Pecaut \& Mamajek 2013b})$). At a distance of $\sim 320\text{pc}$, the companion has a projected separation of $\sim 250\text{au}$. Interestingly, TOI-2152 also has another companion further out detected by *Gaia* with an angular separation of ~ 20 arcsec ($\sim 6000\text{au}$; see Section 2.7).

2.7 Gaia assessment

In addition to the high-resolution imaging, we have utilized *Gaia* to identify any wide stellar companions that may be bound members of the system. Typically, these stars are already in the *TESS* Input Catalog and their flux dilution to the transit has already been accounted for in the transit fits and associated derived parameters. Based upon similar parallaxes and proper motions (Mugrauer & Michel 2020, 2021), the only TOI in our sample which appears to have a wide stellar companion is TOI-2152 (in addition to the close-in companion identified in Section 2.6.2); the wide companion TIC 395 393 263 (*Gaia* DR3 562112709676597376) is 20 arcsec to the NW ($PA \approx 300^\circ$) which corresponds to a projected physical separation of ~ 6000 au. The companion has a mass and temperature consistent with an M4V star ($M \sim 0.24M_\odot; T_{\text{eff}} \sim 3223\text{K}$ Mugrauer & Michel 2021) – for such a small star at such a large separation, the stellar companion does not affect the stability of the planets or the measured radial velocities. Interestingly, the projected positions on the sky of the three stars are not in a line indicating that the mutual inclination of the two stellar companions is non-zero – astrometric and/or radial velocity observations would be needed to determine if the transiting planet is aligned or not with either of the two stellar companions. A summary of the hierarchical triple TOI-2152 is given in Table 5.

Gaia DR3 astrometry (*Gaia* Collaboration et al. 2021) provides additional information on the possibility of inner companions that may have gone undetected by either *Gaia* DR2 data or the high resolution imaging. The *Gaia* Renormalized Unit Weight Error (RUWE) is a metric, similar to a reduced chi-square, where values that are $\lesssim 1.4$ indicate that the *Gaia* astrometric solution is consistent with the star being single whereas RUWE values $\gtrsim 1.4$ may indicate an astrometric excess noise, possibly caused the presence of an unseen companion (e.g. Ziegler et al. 2020). All of the TOIs in this sample,

Table 5. Estimated parameters for TOI-2152 stellar components.

Stellar Component	Separation [au]	Mass [M_\odot]	Radius [R_\odot]	T_{eff} [K]	Spectral Type	Notes
TOI-2152A	...	1.52	1.61	6630	F4V	Table 6
TOI-2152B	250	0.5	0.4	3600	M1V	Boyajian et al. (2012); Pecaut & Mamajek (2013a)
TOI-2152C	6000	0.24	0.2	3200	M4V	Boyajian et al. (2012); Mugrauer & Michel (2020)

Table 6. Median values and 68 % confidence intervals for the global models.

Parameter	Units	TOI-1811 b	TOI-2025 b	TOI-2145 b	TOI-2152A b	TOI-2154 b	TOI-2497 b
<i>π</i> Gaia Parallax (mas)		7.800 ± 0.051	2.9775 ± 0.0312	4.4509 ± 0.0314	3.3018 ± 0.0417	3.3744 ± 0.0337	3.5072 ± 0.0508
[Fe/H] Metallicity (dex)		0.27 ± 0.08	0.19 ± 0.08	0.23 ± 0.08	0.27 ± 0.08	0.02 ± 0.08	0.06 ± 0.08
<i>A_v</i> V-band extinction (mag)		0.04619	0.1801	0.1004	2.0150	0.2793	1.3020
<i>T_c</i> * Time of conjunction (BJD _{TDB})		2454006.04900 ± 0.00337	—	—	—	—	—
<i>D_T</i> Dilution in TESS		0.00000 ± 0.00028	0.00000 ± 0.00026	—	0.00000 ± 0.02032	0.00000 ± 0.00055	—
Parameter	Units	Values	Values	Values	Values	Values	Values
Stellar parameters:							
<i>M_*</i>		0.817 ^{+0.033} _{-0.030}	1.199 ^{+0.074} _{-0.092}	1.720 ^{+0.057} _{-0.075}	1.516 ^{+0.085} _{-0.10}	1.233 ^{+0.077} _{-0.090}	1.859 ^{+0.087} _{-0.083}
<i>R_*</i>		0.769 ^{+0.019} _{-0.019}	1.459 ^{+0.043} _{-0.043}	2.749 ^{+0.066} _{-0.066}	1.612 ^{+0.056} _{-0.056}	1.396 ^{+0.049} _{-0.043}	2.36 ^{+0.12} _{-0.11}
<i>R_*</i> , SED		0.7717 ^{+0.0074} _{-0.0074}	1.498 ± 0.018	2.792 ^{+0.029} _{-0.028}	1.621 ^{+0.038} _{-0.038}	1.400 ± 0.020	2.365 ± 0.046
<i>L_*</i>		0.2753 ^{+0.0071} _{-0.0070}	2.44 ^{+0.12} _{-0.11}	9.92 ± 0.33	4.50 ^{+0.77} _{-0.64}	2.72 ^{+0.23} _{-0.20}	14.7 ^{+2.0} _{-1.7}
<i>F_{bol}</i>		0.536 ± 0.012	0.693 ^{+0.033} _{-0.028}	6.29 ^{+0.18} _{-0.22}	1.57 ^{+0.26} _{-0.22}	0.992 ^{+0.080} _{-0.071}	5.77 ^{+0.76} _{-0.65}
<i>ρ_*</i>		2.54 ^{+0.17} _{-0.17}	0.542 ^{+0.062} _{-0.056}	0.1161 ^{+0.0090} _{-0.0091}	0.511 ^{+0.062} _{-0.062}	0.639 ^{+0.083} _{-0.083}	0.200 ^{+0.034} _{-0.034}
log <i>g</i>		4.579 ^{+0.022} _{-0.022}	4.187 ^{+0.037} _{-0.040}	3.794 ^{+0.023} _{-0.027}	4.205 ^{+0.038} _{-0.048}	4.239 ^{+0.042} _{-0.051}	3.962 ^{+0.080} _{-0.049}
<i>T_{eff}</i>		4766 ⁺⁵² ₋₅₄	5977 ⁺⁷⁹ ₋₇₈	6177 ± 67	6630 ⁺³⁰⁰ ₋₂₉₀	6280 ± 160	7360 ⁺³²⁰ ₋₃₀₀
<i>T_{eff}</i> , SED		4760 ⁺²⁰ ₋₁₉	5896 ⁺⁸¹ ₋₆₉	6134 ⁺⁴² ₋₅₃	6610 ⁺³²⁰ ₋₃₀₀	6270 ⁺¹⁵⁰ ₋₁₄₀	7350 ⁺²⁷⁰ ₋₂₅₀
[Fe/H] ₀		0.306 ^{+0.076} _{-0.077}	0.15 ^{+0.11} _{-0.10}	0.247 ^{+0.074} _{-0.072}	0.282 ^{+0.075} _{-0.079}	0.101 ^{+0.071} _{-0.059}	0.094 ^{+0.076} _{-0.072}
Initial Metallicity		0.280 ^{+0.074} _{-0.076}	0.200 ^{+0.055} _{-0.058}	0.286 ^{+0.050} _{-0.056}	0.368 ^{+0.053} _{-0.070}	0.105 ^{+0.059} _{-0.056}	0.177 ^{+0.075} _{-0.074}
Age (Gyr)		5.9 ^{+4.9} _{-4.9}	4.5 ^{+2.3} _{-1.5}	1.80 ^{+0.33} _{-0.23}	0.83 ^{+0.1} _{-0.58}	2.9 ^{+2.1} _{-1.5}	1.00 ^{+0.22} _{-0.19}
EEPS [†]		335 ⁺¹⁵ ₋₃₃	407 ⁺²⁹ ₋₃₅	402.2 ⁺¹¹ _{-8.7}	328 ⁺²² ₋₃₅	369 ⁺⁴⁶ ₋₃₃	360.4 ⁺¹² _{-9.7}
<i>A_v</i>		0.024 ^{+0.015} _{-0.016}	0.079 ^{+0.058} _{-0.050}	0.071 ^{+0.022} _{-0.035}	0.98 ^{+0.17} _{-0.18}	0.137 ^{+0.088} _{-0.087}	0.52 ± 0.13
<i>σ_{SED}</i>		0.86 ^{+0.35} _{-0.21}	0.50 ^{+0.21} _{-0.13}	0.92 ^{+0.33} _{-0.21}	1.09 ^{+0.49} _{-0.25}	0.67 ^{+0.27} _{-0.16}	0.70 ^{+0.38} _{-0.16}
<i>σ</i>	SED photometry error scaling	7.800 ^{+0.050} _{-0.051}	2.978 ± 0.031	4.451 ± 0.031	3.302 ± 0.042	3.374 ± 0.034	3.507 ^{+0.050} _{-0.051}
<i>d</i>	Distance (pc)	128.21 ^{+0.84} _{-0.82}	335.8 ± 3.5	224.7 ± 1.6	302.8 ^{+3.9} _{-3.8}	296.5 ^{+3.0} _{-2.9}	285.1 ^{+4.2} _{-4.0}
Planetary parameters:							
<i>P</i>	Period (days)	3.7130765 ± 0.0000017	8.8720982 ± 0.0000077	10.26075 ^{+0.00083} _{-0.00082}	3.3773512 ^{+0.000060} _{-0.000061}	3.8240801 ± 0.0000025	10.655669 ± 0.000038
<i>R_p</i>	Radius (<i>R_J</i>)	0.994 ^{+0.025} _{-0.023}	1.061 ^{+0.033} _{-0.031}	1.069 ^{+0.029} _{-0.028}	1.281 ^{+0.050} _{-0.046}	1.453 ^{+0.053} _{-0.048}	0.94 ^{+0.059} _{-0.049}
<i>M_p</i>	Mass (<i>M_J</i>)	0.972 ^{+0.028} _{-0.028}	3.60 ± 0.33	5.26 ^{+0.37} _{-0.37}	2.83 ^{+0.37} _{-0.37}	0.92 ^{+0.18} _{-0.18}	4.82 ± 0.41
<i>T_c</i>	Time of conjunction (BJD _{TDB})	2458899.87080 ^{+0.00019} _{-0.00018}	2458690.28895 ± 0.00043	2459013.2808 ± 0.0011	2458792.55575 ± 0.00034	2458819.73080 ^{+0.0011} _{-0.00079}	2459205.0992 ^{+0.0011} _{-0.0010}
<i>T₀</i>	Optimal conjunction Time (BJD _{TDB})	2459126.36846 ^{+0.00017} _{-0.00014}	2459089.53337 ± 0.00025	2459023.54156 ^{+0.00071} _{-0.00070}	2458927.64980 ± 0.00023	2459148.60166 ^{+0.0011} _{-0.00072}	2459109.19818 ^{+0.0011} _{-0.0010}
<i>a</i>	Semi-major axis (AU)	0.04389 ^{+0.00068} _{-0.00055}	0.0892 ^{+0.0018} _{-0.0023}	0.1108 ^{+0.0012} _{-0.0016}	0.05064 ^{+0.00093} _{-0.0011}	0.0513 ^{+0.0011} _{-0.0013}	0.1166 ± 0.0018
<i>i</i>	Inclination (Degrees)	86.48 ^{+0.20} _{-0.20}	88.65 ^{+0.12} _{-0.02}	88.1 ^{+1.2} _{-1.2}	86.42 ^{+0.85} _{-0.85}	83.37 ^{+0.75} _{-0.75}	88.16 ^{+1.1} _{-1.1}
<i>e</i>	Eccentricity	0.052 ^{+0.062} _{-0.037}	0.394 ^{+0.038} _{-0.038}	0.208 ^{+0.034} _{-0.047}	0.057 ^{+0.068} _{-0.040}	0.117 ^{+0.10} _{-0.079}	0.195 ^{+0.043} _{-0.040}
<i>τ_{circ}</i>	Tidal circularization timescale (Gyr)	0.74 ^{+0.13} _{-0.15}	20.6 ⁺¹² _{-7.7}	240 ⁺⁷² ₋₅₉	0.60 ^{+0.18} _{-0.17}	0.129 ^{+0.061} _{-0.050}	410 ⁺⁵⁰ ₋₁₃₀
<i>ω_*</i>	Argument of Periastron (Degrees)	21 ⁺³⁵ ₋₃₃	91.8 ^{+9.9} _{-9.6}	93 ⁺¹¹ ₋₁₃	96 ⁺⁸³ ₋₈₉	31 ⁺⁹⁸ ₋₃₆	-20 ⁺¹⁸ ₋₁₇
<i>T_{eq}</i>	Equilibrium temperature (K)	962.2 ^{+7.9} _{-7.9}	1166 ⁺¹⁸ ₋₁₈	1484 ⁺¹⁶ ₋₁₄	1802 ⁺⁵⁴ ₋₅₄	1580 ± 27	1595 ⁺²⁵ ₋₂₅
<i>K</i>	RV semi-amplitude (m/s)	146 ± 11	341 ⁺²⁸ ₋₂₇	350 ⁺²³ ₋₂₁	291 ± 36	105 ± 21	300 ⁺²³ ₋₂₄
<i>R_p/R_*</i>	Radius of planet in stellar radii	0.13272 ^{+0.00072} _{-0.00071}	0.07469 ^{+0.00052} _{-0.00044}	0.03996 ^{+0.00044} _{-0.00040}	0.0816 ± 0.0012	0.10693 ^{+0.00095} _{-0.00090}	0.04333 ^{+0.00058} _{-0.00051}
<i>a/R_*</i>	Semi-major axis in stellar radii	12.28 ^{+0.27} _{-0.31}	13.12 ± 0.48	8.65 ^{+0.22} _{-0.23}	6.76 ^{+0.26} _{-0.31}	7.91 ^{+0.33} _{-0.37}	10.63 ^{+0.58} _{-0.55}
<i>Depth₁</i>	Flux decrement at mid transit	0.01761 ± 0.00019	0.005578 ^{+0.00078} _{-0.00065}	0.001597 ^{+0.00085} _{-0.00082}	0.00666 ^{+0.00080} _{-0.00065}	0.01143 ^{+0.00080} _{-0.00079}	0.001877 ^{+0.00069} _{-0.00064}
<i>Depth₂</i>	Flux decrement at mid transit for TESS	0.01802 ± 0.00014	0.006324 ^{+0.00079} _{-0.00079}	—	0.00728 ^{+0.00018} _{-0.00017}	0.01046 ^{+0.00015} _{-0.00014}	0.002013 ± 0.000044
<i>τ</i>	Ingress/egress transit duration (days)	0.01918 ^{+0.00065} _{-0.00064}	0.01078 ^{+0.00092} _{-0.00036}	0.01260 ^{+0.0016} _{-0.00063}	0.0140 ± 0.0019	0.0345 ^{+0.0023} _{-0.0022}	0.0154 ^{+0.0030} _{-0.0017}
<i>T₁₄</i>	Total transit duration (days)	0.08128 ^{+0.00057} _{-0.00056}	0.15003 ^{+0.00099} _{-0.00084}	0.3103 ^{+0.0021} _{-0.0019}	0.1548 ^{+0.0017} _{-0.0016}	0.1027 ± 0.0010	0.3266 ^{+0.0031} _{-0.0027}
<i>b</i>	Transit Impact parameter	0.7393 ^{+0.0083} _{-0.0083}	0.19 ^{+0.14} _{-0.14}	0.23 ± 0.16	0.415 ^{+0.098} _{-0.098}	0.8636 ^{+0.0091} _{-0.0091}	0.35 ^{+0.16} _{-0.16}
<i>T_{5,14}</i>	Total eclipse duration (days)	0.08168 ^{+0.00060} _{-0.00077}	0.314 ^{+0.041} _{-0.058}	0.452 ^{+0.041} _{-0.057}	0.1606 ^{+0.023} _{-0.0089}	0.0965 ^{+0.0072} _{-0.024}	0.292 ^{+0.030} _{-0.028}

Table 6 – continued

Priors:	TOI-1811 b	TOI-2025 b	TOI-2145 b	TOI-2152A b	TOI-2154 b	TOI-2497 b
ρ_p	$1.23^{+0.13}_{-0.12}$	$3.74^{+0.51}_{-0.46}$	$5.34^{+0.59}_{-0.54}$	$1.67^{+0.31}_{-0.29}$	$0.370^{+0.092}_{-0.081}$	$6.1^{+1.2}_{-1.1}$
$\log g_p$	$3.387^{+0.038}_{-0.041}$	$3.899^{+0.047}_{-0.050}$	$4.057^{+0.038}_{-0.039}$	$3.630^{+0.065}_{-0.072}$	$3.032^{+0.088}_{-0.10}$	$4.082^{+0.059}_{-0.063}$
T_5	$2458898.100^{+0.089}_{-0.089}$	$2458694.65^{+0.40}_{-0.41}$	$2459018.34^{+0.28}_{-0.27}$	$2458794.241^{+0.084}_{-0.099}$	$2458817.94^{+0.137}_{-0.23}$	$2459200.96^{+0.24}_{-0.24}$
$\text{ecos}\omega_*$	$0.036^{+0.070}_{-0.038}$	$-0.012^{+0.065}_{-0.067}$	$-0.010^{+0.042}_{-0.040}$	$-0.002^{+0.039}_{-0.046}$	$0.051^{+0.15}_{-0.094}$	$0.176^{+0.034}_{-0.035}$
$\text{esin}\omega_*$	$0.015^{+0.029}_{-0.021}$	$0.388^{+0.035}_{-0.038}$	$0.203^{+0.034}_{-0.047}$	$0.022^{+0.076}_{-0.039}$	$0.035^{+0.054}_{-0.042}$	$-0.064^{+0.059}_{-0.067}$
d/R_*	$12.04^{+0.53}_{-0.68}$	$8.00^{+0.75}_{-0.71}$	$6.91^{+0.49}_{-0.43}$	$6.58^{+0.48}_{-0.68}$	$7.48^{+0.69}_{-0.77}$	$10.97^{+1.1}_{-0.97}$

Notes. See Table 3 in Eastman et al. (2019) for a detailed description of all derived and fitted parameters.

** T_c prior comes from analysis of the WASP photometry (see Section 2.3). We note that this time is in HD_{DR8} while all data files and results here are BJDR₈. The difference between these two time systems is on the order of seconds while the precision on T_c used as a prior is on order of minutes, and therefore has no influence on the results.

†We assume the TESS correction for blending is much better than 10%. We use a prior of 10% of the determined blending from TICv8 (Stassun et al. 2018).

‡The initial metallicity is the metallicity of the star when it was formed.

§The Equal Evolutionary Point corresponds to static points in a stars evolutionary history when using the MIST isochrones and can be a proxy for age. See §2 in Dotter (2016) for a more detailed description of EEP.

*Optimal time of conjunction minimizes the covariance between T_c and Period. This is the transit mid-point.

††The tidal quality factor (Q_2) is assumed to be 10^6 .

except TOI 1811, have RUWE values of <1.1 indicating that the astrometric fits are consistent with the single star model. The RUWE for TOI-1811 is 1.66; there is no clear fixed boundary for when the RUWE unambiguously identifies the presence of an unseen stellar companion. The transit of TOI-1811 is very deep (19 mmag in the *TESS* light curves) and with a short orbital period of 3.7 d, it may be the transit of the planet itself that is affecting the *Gaia* RUWE value.

3 EXOFASTV2 GLOBAL FITS

Following the same strategy laid out in §3 of Rodriguez et al. (2021), we globally fit the RVs, *TESS*, and TFOP photometry (see Figs 3, 4, & 5; and Section 2) for TOI-1811 b, TOI-2025 b, TOI-2145 b, TOI-2152A b, TOI-2154 b, and TOI-2497 b with EXOFASTv2 (Eastman, Gaudi & Agol 2013; Eastman et al. 2019) to determine their individual system parameters and place them in context with the known exoplanet population. To ensure that none of the SG1 partial transits are influencing the results for any system, we run fits with and without partial transits and the fitted system parameters are consistent ($<1\sigma$). The SG1 photometry provides a strong constrain on the transit ephemerides of these systems by significantly extending the baseline of the observations. The spectral energy distribution (SED) and the MESA Isochrones and Stellar Tracks (MIST) stellar evolution models (Paxton et al. 2011, 2013, 2015; Choi et al. 2016; Dotter 2016) were included to constrain the host star’s parameters within the fit, and we account for the 30 minute smearing in the *TESS* FFI lightcurves. We enforced a systematic limit on the precision broad-band photometry (see Table 1, Stassun & Torres 2016) and use EXOFASTv2’s default lower limit on the systematic error on the bolometric flux ($F_{\text{bol}} \sim 3$ per cent). We adopted a Gaussian prior on the [Fe/H], parallax from *Gaia* DR2 (*Gaia* Collaboration et al. 2016, 2018, correcting for the offset reported by Lindegren et al. 2018), and an upper bound on the line of sight extinction from Schlegel, Finkbeiner & Davis (1998) & Schlafly & Finkbeiner (2011). Both SPOC and our custom pipeline correct the *TESS* photometry for known nearby blended stars in the aperture. To allow some flexibility while checking this correction, we fit for dilution term on the *TESS* band, and placed a Gaussian prior of 0 ± 10 per cent of the contamination ratio reported by the *TESS* Input Catalog (TIC, Stassun et al. 2018). We saw no evidence of any significant dilution in TOI-1811, TOI-2025, TOI-2152, and TOI-2154. Unfortunately, without an independent full transit for TOI-2145 and TOI-2497, we are not able to perform this test with the limited amount of photometric follow-up. We use the recommended convergence criteria by Eastman et al. (2019) of a Gelman-Rubin statistic (<1.01) and independent draws (>1000). The results for each system are in Tables 6, 7, and 8 and in Figs 3, 4, and 5.

4 DISCUSSION

The combination of precision, baseline, and cadence of *TESS* will provide the ability to create a magnitude-complete, self-consistent catalog of exoplanetary systems to investigate questions about formation and evolution, and directly test tentative trends seen in the current population (Nelson, Ford & Rasio 2017; Rodriguez et al. 2021; Ikwut-Ukwa et al. 2022). These six new hot and warm giant planets increase the current sample of systems with precise mass and eccentricity measurements. We first review our results on each system and then discuss the impact *TESS* has made on the field of giant exoplanets. In all six systems, we see no significant inflation

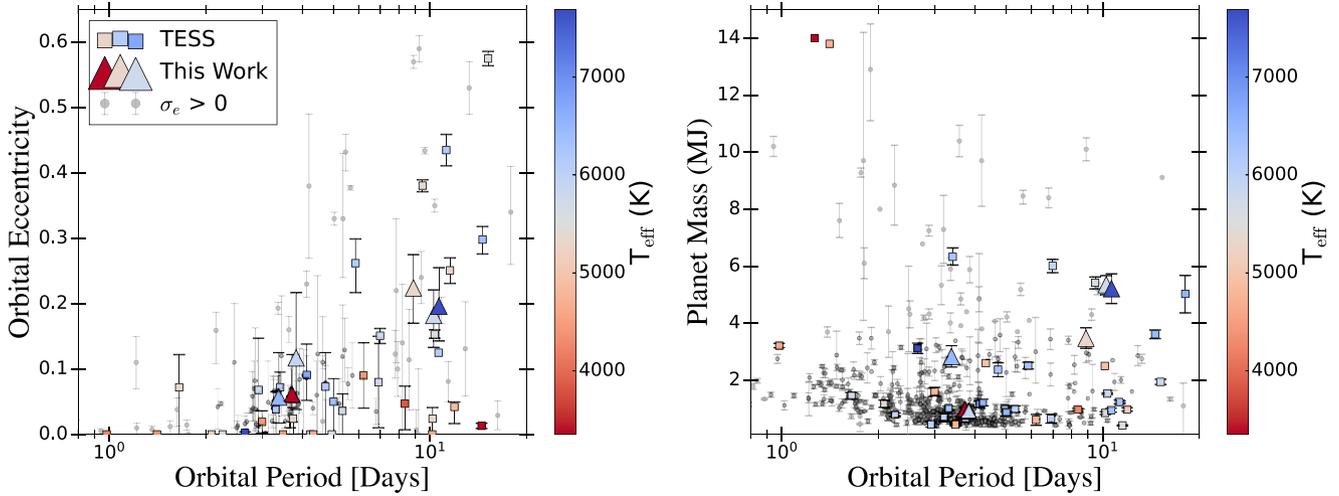


Figure 6. (Left) The eccentricity and log of the orbital period of all known giant planets with a mass greater than $0.4 M_J$ with period between 0.8 and 30 d. The systems with a measured eccentricity from the NASA Exoplanet Archive (NEA) are shown as grey circles with errors. (Right) The mass and log of the orbital period of all known transiting giant planets. In both figures the *TESS*-discovered systems (including the ones presented in this work) are the squares colored by the host star’s effective temperature (with those from this work are displayed with a triangle symbol), showing the diversity of the host stars in the *TESS* giant planet sample.

($R_p > 1.5 R_\odot$). We also see some significant reddening for TOI-2152 and TOI-2497 from our global fit (see Table 6).

4.1 Review of six new discoveries

Orbiting an early K-star, TOI-1811 b is a hot Jupiter on a 3.71 day orbital period that shows no signs of inflation relative to the known population ($R_p = 0.994^{+0.025}_{-0.023} R_J$ and $M_p = 0.972^{+0.076}_{-0.078} M_J$). The host star has a relatively high metallicity ($[Fe/H] = 0.306^{+0.076}_{-0.077}$ dex), and the lack of a significant eccentricity is consistent with the very short tidal circularization time-scale of 740^{+13}_{-15} Myr (Adams & Laughlin 2006) and that the host star parameters suggest a main-sequence star with an age well above this.

TOI-2025 b is a super Jupiter mass ($M_p = 3.60 \pm 0.33 M_J$) planet on an 8.872 day orbital period around an early-G star. We detect a moderate, but significant eccentricity, $e = 0.394^{+0.035}_{-0.038}$. Given the long circularization time-scale (see Table 6) and the detected eccentricity, it is possible that TOI-2025 b migrated to its current location through dynamical interactions (e.g. Dawson & Fabrycky 2010).

Orbiting a bright ($G = 8.94 \pm 0.02$ mag), sub-giant ($\log g = 3.794^{+0.023}_{-0.027}$ cgs), TOI-2145 is a massive ($M_p = 5.26^{+0.38}_{-0.37} M_J$) warm Jupiter on an eccentric ($e = 0.208^{+0.034}_{-0.047}$) on a 10.261 day orbit. Of the known transiting planets to date, TOI-2145 b joins only five other known planets to have a mass above $3 M_J$ and orbit a subgiant ($\log g < 4.0$ cgs), but it orbits the brightest star of that group, a valuable aspect for future detailed characterization.

TOI-2152A b and TOI-2154 b are both hot Jupiters orbiting similar main-sequence F-stars at similar distances from the Sun. TOI-2152A b is a massive Jupiter ($M_p = 2.83^{+0.38}_{-0.37} M_J$) while TOI-2154 b is only $0.92^{+0.19}_{-0.18} M_J$. We see no evidence of any significant eccentricity (TOI-2152A b $e = 0.057^{+0.068}_{-0.040}$, TOI-2154 b $e = 0.117^{+0.10}_{-0.079}$) from our results but note that these two planets provide a nice comparative study since their host stars and the planets share many similar characteristics, but exhibit a significant difference in the planet’s mass.

The last system in our sample is TOI-2497 b, another very massive ($M_p = 5.21 \pm 0.52 M_J$) warm Jupiter on a 10.656 day orbital period. Its host star, TOI-2497, is a rapidly rotating ($v \sin I_* = 39.6 \pm 1.0$

km s^{-1}) early F-star ($T_{\text{eff}} = 7360^{+320}_{-300}$, that has possibly left the main sequence ($\log g = 3.962^{+0.050}_{-0.049}$ cgs). The host star is also bright ($G = 9.47 \pm 0.02$ mag), and combined with the rapid rotation, TOI-2497 b is an excellent target for future Doppler spectroscopy, using observations of the Rossiter McLaughlin effect (McLaughlin 1924; Rossiter 1924) or Doppler tomography (e.g. Miller et al. 2010; Johnson et al. 2014; Zhou et al. 2016) to measure the projected spin-orbit alignment of the planet’s orbit.

4.2 *TESS*’s impact on giant planets

As NASA’s *TESS* mission continues to observe, it is expected to discover thousands of giant planets over its lifetime (Sullivan et al. 2015; Barclay, Pepper & Quintana 2018) while providing great value to already known systems (Ikwut-Ukwa et al. 2020; Edwards et al. 2021; Kane et al. 2021). This is highly dependent on the number of extended missions that *TESS* is given. Even in the ~ 4 yr since its launch, *TESS* has discovered over 200 planets¹⁰, of which 47 are above $0.4 M_J$, nearly 10 per cent of the known transiting giant planet population (See Fig. 6). As multiple efforts, including ours, continue to confirm and characterize new transiting giant planets, it will lead to a magnitude-complete, self-consistent sample of planet properties (Zhou et al. 2019; Yee et al. 2021).

There is an obvious trend in the eccentricity distribution of giant planets, where long period giant planets tend to have a wider distribution of orbital eccentricities than shorter period systems, possibly indicative of the system’s migration history. If a planet migrates to a close-in configuration through dynamical interactions with other bodies, it can result in a highly eccentric and/or misaligned orbit (Rasio & Ford 1996; Wu & Lithwick 2011). Specifically, looking at Fig. 6, we see that the eccentricity range appears to broaden beyond an orbital period of ~ 3 d. We note that many components of a planet’s formation and evolutionary history are incorporated into this distribution, and a proper analysis of the population as a

¹⁰<https://exoplanetarchive.ipac.caltech.edu>, accessed April 2022

Table 7. Median values and 68 % confidence intervals for the global models.

TOI-1811		B		R		g'		i'	
Wavelength parameters:		r'		z'		TESS		V	
t_1	linear limb-darkening coeff	0.944 ± 0.037	$0.665^{+0.045}_{-0.046}$	$0.665^{+0.045}_{-0.046}$	$0.941^{+0.041}_{-0.042}$	$0.941^{+0.041}_{-0.042}$	$0.482^{+0.023}_{-0.022}$	$0.482^{+0.023}_{-0.022}$	0.746 ± 0.050
t_2	quadratic limb-darkening coeff	-0.108 ± 0.037	0.394 ± 0.033	$0.203^{+0.046}_{-0.047}$	$-0.032^{+0.045}_{-0.046}$	$-0.032^{+0.045}_{-0.046}$	0.171 ± 0.022	0.171 ± 0.022	$0.055^{+0.080}_{-0.051}$
A_b	Dilution from neighboring stars	$0.090^{+0.044}_{-0.045}$	0.196 ± 0.033	0.196 ± 0.033	0.130 ± 0.043	0.130 ± 0.043	—	—	—
Telescope Parameters:		TRES		—		—		—	
γ_{rel}	Relative RV Offset (m/s)	$-187.0^{+9.1}_{-9.7}$	—	—	—	—	—	—	—
σ_J	RV Jitter (m/s)	17^{+17}_{-17}	—	—	—	—	—	—	—
σ_J^2	RV Jitter Variance	300^{+690}_{-320}	—	—	—	—	—	—	—
Transit Parameters:		TESS		LCOHAL0m4 UT 2020-04-23 (i')		LCOSSO0m4 UT 2020-04-23 (i')		BYU UT 2020-04-27 (R)	
σ^2	ULMT UT 2020-04-27 (i')	Montcabrer UT 2020-04-30 (i')	BYU12in UT 2020-05-08 (V)	BYU12in UT 2020-05-08 (V)	EISauce UT 2020-05-12 (B)	EISauce UT 2020-05-12 (B)	EISauce UT 2020-05-12 (B)	LCOSSO1m UT 2021-02-25 (B)	LCOSSO1m UT 2021-02-25 (B)
	LCOSSO1m UT 2021-02-25 (z')	MUSCAT2 UT 2021-06-05 (g')	MUSCAT2 UT 2021-06-05 (i')	MUSCAT2 UT 2021-06-05 (i')	MUSCAT2 UT 2021-06-05 (r')	MUSCAT2 UT 2021-06-05 (r')	MUSCAT2 UT 2021-06-05 (r')	MUSCAT2 UT 2021-06-05 (z')	MUSCAT2 UT 2021-06-05 (z')
	Added Variance $\times 10^{-5}$	$0.034^{+0.19}_{-0.16}$	$5.8^{+1.2}_{-1.0}$	$5.8^{+1.2}_{-1.0}$	$1.11^{+0.60}_{-0.55}$	$1.11^{+0.60}_{-0.55}$	$1.11^{+0.60}_{-0.55}$	$0.082^{+0.067}_{-0.057}$	$0.082^{+0.067}_{-0.057}$
	$0.098^{+0.034}_{-0.027}$	$0.34^{+0.16}_{-0.16}$	$2.10^{+0.33}_{-0.33}$	$2.10^{+0.33}_{-0.33}$	$1.18^{+0.43}_{-0.42}$	$1.18^{+0.43}_{-0.42}$	$1.18^{+0.43}_{-0.42}$	$0.20^{+0.099}_{-0.099}$	$0.20^{+0.099}_{-0.099}$
	$1.18^{+0.31}_{-0.25}$	$-0.027^{+0.055}_{-0.055}$	$0.061^{+0.057}_{-0.057}$	$0.061^{+0.057}_{-0.057}$	$-0.028^{+0.046}_{-0.046}$	$-0.028^{+0.046}_{-0.046}$	$-0.028^{+0.046}_{-0.046}$	$-0.079^{+0.054}_{-0.054}$	$-0.079^{+0.054}_{-0.054}$
F_0	Baseline flux	1.000031 ± 0.000060	$1.00236^{+0.00081}_{-0.00079}$	$1.00236^{+0.00081}_{-0.00079}$	$1.01023^{+0.00068}_{-0.00066}$	$1.01023^{+0.00068}_{-0.00066}$	$1.01023^{+0.00068}_{-0.00066}$	1.00007 ± 0.00021	1.00007 ± 0.00021
C_0	Additive detrending coeff	0.99881 ± 0.00016	1.00856 ± 0.00034	1.00856 ± 0.00034	0.99772 ± 0.00061	0.99772 ± 0.00061	0.99772 ± 0.00061	$0.99526^{+0.00033}_{-0.00034}$	$0.99526^{+0.00033}_{-0.00034}$
	0.00512 \pm 0.00041	1.00004 ± 0.00019	1.00016 ± 0.00017	1.00016 ± 0.00017	0.99991 ± 0.00015	0.99991 ± 0.00015	0.99991 ± 0.00015	1.00056 ± 0.00019	1.00056 ± 0.00019
	0.0010 \pm 0.0013	—	0.0074 ± 0.0023	0.0074 ± 0.0023	-0.0036 ± 0.0022	-0.0036 ± 0.0022	-0.0036 ± 0.0022	0.00381 ± 0.00052	0.00381 ± 0.00052
	—	$0.00186^{+0.00061}_{-0.00063}$	$-0.0039^{+0.00012}_{-0.00013}$	$-0.0039^{+0.00012}_{-0.00013}$	$0.0053^{+0.00018}_{-0.00019}$	$0.0053^{+0.00018}_{-0.00019}$	$0.0053^{+0.00018}_{-0.00019}$	$0.000816^{+0.00087}_{-0.00088}$	$0.000816^{+0.00087}_{-0.00088}$
TOI-2025		Kepler		Kepler		R		g'	
Wavelength Parameters:		TESS		TESS		R		V	
t_1	linear limb-darkening coeff	0.611 ± 0.053	0.416 ± 0.036	0.416 ± 0.036	0.346 ± 0.050	0.346 ± 0.050	$0.556^{+0.085}_{-0.084}$	$0.556^{+0.085}_{-0.084}$	—
t_2	quadratic limb-darkening coeff	0.283 ± 0.037	0.247 ± 0.026	0.247 ± 0.026	0.432 ± 0.039	0.432 ± 0.039	$0.236^{+0.081}_{-0.082}$	$0.236^{+0.081}_{-0.082}$	—
A_b	Dilution from neighboring stars	0.178 ± 0.053	0.310 ± 0.035	0.310 ± 0.035	$0.300^{+0.049}_{-0.050}$	$0.300^{+0.049}_{-0.050}$	—	—	—
	—	0.296 ± 0.036	0.273 ± 0.028	0.273 ± 0.028	0.277 ± 0.037	0.277 ± 0.037	—	—	—
	—	$0.00001^{+0.00026}_{-0.00025}$	—	—	—	—	—	—	—
Telescope Parameters:		TRES		TRES		SCT		SCT	
γ_{rel}	Relative RV Offset (m/s)	189 ± 19	—	—	—	—	—	—	—
σ_J	RV Jitter (m/s)	61^{+22}_{-22}	—	—	—	—	—	—	—
σ_J^2	RV Jitter Variance	3800^{+5200}_{-1800}	—	—	—	—	—	—	—
Transit Parameters:		TESS S40		TESS S40		LCOTEN UT 2020-06-26 (i')		SCT UT 2020-06-26 (TESS)	
σ^2	MORP UT 2021-09-30 (Kepler)	TESS S14,18,19,20,24,25,26	KeplerCam UT 2021-05-12 (i')	KeplerCam UT 2021-05-12 (i')	GMU UT 2021-05-20 (V)	GMU UT 2021-05-20 (V)	GMU UT 2021-05-20 (V)	GMU UT 2021-05-21 (R)	GMU UT 2021-05-21 (R)
	Added Variance $\times 10^{-5}$	$-0.0064^{+0.0012}_{-0.0011}$	0.000005 ± 0.000021	0.000005 ± 0.000021	0.99954 ± 0.00044	0.99954 ± 0.00044	0.99954 ± 0.00044	0.99977 ± 0.00028	0.99977 ± 0.00028
	$-0.0035^{+0.0097}_{-0.0097}$	$0.527^{+0.087}_{-0.087}$	1.00386 ± 0.00019	1.00386 ± 0.00019	$1.00051^{+0.00039}_{-0.00038}$	$1.00051^{+0.00039}_{-0.00038}$	$1.00051^{+0.00039}_{-0.00038}$	1.000387 ± 0.00019	1.000387 ± 0.00019
	$0.554^{+0.053}_{-0.049}$	$0.370^{+0.048}_{-0.044}$	0.99799 ± 0.00012	0.99799 ± 0.00012	0.00283 ± 0.00096	0.00283 ± 0.00096	0.00283 ± 0.00096	-0.00070 ± 0.00080	-0.00070 ± 0.00080
F_0	Baseline flux	1.000005 ± 0.000021	1.00379 ± 0.00029	1.00379 ± 0.00029	1.00293 ± 0.00029	1.00293 ± 0.00029	1.00293 ± 0.00029	0.99977 ± 0.00028	0.99977 ± 0.00028
C_0	Additive detrending coeff	1.00023 ± 0.00014	0.99799 ± 0.00012	0.99799 ± 0.00012	0.00283 ± 0.00096	0.00283 ± 0.00096	0.00283 ± 0.00096	1.000387 ± 0.00019	1.000387 ± 0.00019
	—	-0.00278 ± 0.00045	-0.00195 ± 0.00068	-0.00195 ± 0.00068	$-0.00026^{+0.00088}_{-0.00089}$	$-0.00026^{+0.00088}_{-0.00089}$	$-0.00026^{+0.00088}_{-0.00089}$	-0.00070 ± 0.00080	-0.00070 ± 0.00080
	—	—	$-0.00577^{+0.00085}_{-0.00085}$	$-0.00577^{+0.00085}_{-0.00085}$	—	—	—	$0.00356^{+0.00041}_{-0.00042}$	$0.00356^{+0.00041}_{-0.00042}$

Table 7 – *continued*

TOI-2145		r'	r'	r'	TRES
Wavelength Parameters:					
u_1	linear limb-darkening coeff	0.242 ± 0.051	$0.316^{+0.065}_{-0.065}$	0.220 ± 0.029	
u_2	quadratic limb-darkening coeff	0.314 ± 0.050	0.310 ± 0.050	$0.297^{+0.034}_{-0.033}$	
Telescope Parameters:					
γ_{rel}	Relative RV Offset (m/s)	61 ± 41	MINERVAT2	MINERVAT3	TRES
σ_J	RV Jitter (m/s)	167^{+43}_{-32}	-13^{+27}_{-25}	-50^{+140}_{-180}	-194 ± 16
σ_J^2	RV Jitter Variance	28000^{+16000}_{-11000}	71^{+32}_{-32}	220^{+410}_{-410}	35 ± 22
			5100^{+5600}_{-3100}	47000^{+34000}_{-55000}	1300^{+2100}_{-1100}
Transit Parameters:					
σ^2	Added Variance $\times 10^{-5}$	$0.00435^{+0.00087}_{-0.00073}$	TESS S40	ULMoore UT 2021-09-07 (i')	CRCO UT 2021-09-07 (i')
F_0	Baseline flux	1.000900 ± 0.000012	$0.00273^{+0.00075}_{-0.00073}$	$1.74^{+0.23}_{-0.20}$	$1.221^{+0.092}_{-0.084}$
C_0	Additive detrending coeff	–	1.000627 ± 0.000011	1.00087 ± 0.00036	1.00066 ± 0.00017
			–	$-0.00136^{+0.00070}_{-0.00071}$	-0.00398 ± 0.00040

function of host star parameters is warranted prior to drawing any conclusions. This trend is also seen for brown dwarfs, indicating that more massive systems may undergo migration scenarios similar to planets (Carmichael et al. 2021).

Another possible piece of the puzzle is that a tentative trend has emerged where longer period hot Jupiters (> 5 d) are more massive than shorter period ones (Ikwt-Ukwa et al. 2022). Unfortunately, the lack of homogeneity of the current exoplanet population makes any observed trends difficult to interpret since they may only manifest due to the different assumptions and analysis techniques used. More importantly, Fig. 6 shows the large impact *TESS* is making on the field of giant planets purely from the large number of Jovian-sized planets it has discovered to date, with many of them on longer orbital periods ($P > 5$ d) where the ground-based transit surveys struggled due to poor duty cycles (Gaudi et al. 2005). With the expectation of hundreds of additional discoveries as *TESS* continues to scan the entire sky, the community will have a large number of systems to consider for future detailed characterization using ongoing and future facilities like the James Webb Space Telescope (JWST), the Atmospheric Remote-sensing Infrared Exoplanet Large-survey (ARIEL, Tinetti et al. 2016), and future 30-m class ground-based telescopes. Future work should consider obtaining Doppler spectroscopy on TOI-2497 b to determine the orbital obliquity of the planet, a key aspect related to a planet’s migration history.

5 CONCLUSION

Using a combination of photometric and spectroscopic observations, we present the discovery of six new hot and warm giant planets (TOI-1811 b, TOI-2025 b, TOI-2145 b, TOI-2152A b, TOI-2154 b, and TOI-2497 b). These systems increase the number of giant planets discovered by *TESS* to date and are a part of a larger effort to create a complete sample of systems brighter than $G < 12.5$ in support of future population studies. Of the six systems presented here, we note a few interesting aspects. First, TOI-2145 is a bright ($G = 8.94 \pm 0.02$ mag), subgiant ($\log g = 3.798^{+0.023}_{-0.026}$ cgs) with a 10.26 d period and a $\sim 5 M_J$ planet. Interestingly, we see no signs of inflation from the measured radius of TOI-2145 b, but it is important to note that hot Jupiters discovered around evolved stars suggest planets may re-inflate in the post-main sequence phase (Almenara et al. 2015; Grunblatt et al. 2016; Hartman & Bakos 2016; Stevens et al. 2017; Komacek et al. 2020), when a warm Jupiter (like TOI-2145 b) will receive a similar amount of irradiation to that of a hot Jupiter (Lopez & Fortney 2016). TOI-2152A b and TOI-2154 b are similar orbital period hot Jupiters that orbit similar hosts but the planets are $2.83^{+0.38}_{-0.37} M_J$ and $0.92^{+0.19}_{-0.18} M_J$ providing a nice opportunity for future comparative studies. TOI-2497 b orbits a massive, early F-star ($T_{\text{eff}} = 7360^{+290}_{-270}$), and the combination of its host star’s brightness ($G = 9.47 \pm 0.02$ mag) and rotation period ($v \sin I_* = 39.6 \pm 1.0$ km s $^{-1}$) make it well-suited for orbital obliquity measurements through transit spectroscopy followup. *TESS* continues to discover a wealth of transiting giant planets that may provide insight into their formation and evolutionary mechanisms.

ACKNOWLEDGEMENTS

LC, KS, EA, JR, JER, JAR, PW, and EZ are grateful for support from NSF grants AST-1751874 and AST-1907790, along with a Cottrell Fellowship from the Research Corporation. CZ is supported by a Dunlap Fellowship at the Dunlap Institute for Astronomy & Astrophysics, funded through an endowment established by the Dunlap family and the University of Toronto. T.H. acknowledges

Table 8. Median values and 68 % confidence intervals for the global models.

TOI-2152	B	R	g'	i'
Wavelength Parameters:				
u_1	TESS 0.484 ^{+0.067} _{-0.061}	0.262 ^{+0.047} _{-0.044}	0.423 ^{+0.067} _{-0.064}	0.207 ^{+0.057} _{-0.056}
u_2	0.205 ^{+0.040} _{-0.040}	0.337 ± 0.037	0.287 ^{+0.056} _{-0.057}	0.327 ± 0.050
A_p	0.330 ± 0.049	—	—	—
Telescope Parameters:				
γ_{rel}	—0.001 ± 0.018	—	—	—
σ_J	TESS 207 ⁺²⁹ ₋₂₈	—	—	—
σ_J^2	83 ⁺³⁷ ₋₃₇	—	—	—
σ_J^2	7000 ⁺⁷⁵⁰⁰ ₋₃₇₀₀	—	—	—
Transit Parameters:				
σ^2	TESS Kourouka UT 2020-12-10 (B) CALOU UT 2020-11-24 (B) Added Variance × 10 ⁻⁵ 0.73 ^{+0.39} _{-0.17}	OWL UT 2020-08-17 (R) CRCAO UT 2021-06-28 (R) 1.16 ^{+0.21} _{-0.19} 1.23 ^{+0.13} _{-0.13}	WafflowCreek UT 2020-10-11 (g')	WafflowCreek UT 2020-10-11 (i')
F_0	1.00023 ± 0.000017	1.00036 ± 0.00030	1.00344 ± 0.00038	1.00342 ± 0.00035
C_0	1.00137 ± 0.00032	1.00032 ± 0.00028	—0.00219 ^{+0.00094} _{-0.00093}	—0.00104 ^{+0.00084} _{-0.00085}
C_0	—0.00132 ^{+0.00052} _{-0.00051}	0.00008 ± 0.00044	—	—
TOI-2154				
Wavelength Parameters:				
u_1	B 0.493 ± 0.056	I 0.211 ± 0.052	Kepler 0.325 ± 0.052	z' 0.195 ± 0.038
u_2	0.205 ± 0.054	0.298 ± 0.050	0.306 ^{+0.049} _{-0.050}	0.304 ± 0.035
A_p	—	—	—	—
Telescope Parameters:				
γ_{rel}	—	—	—	—
σ_J	10 ⁺²⁰ ₋₁₈	—	—	—
σ_J^2	32 ⁺²⁶ ₋₃₂	—	—	—
σ_J^2	1000 ⁺¹¹⁰⁰ ₋₁₀₀₀	—	—	—
Transit Parameters:				
σ^2	TESS LCO MeD UT 2020-12-03 (z') —0.1708 ^{+0.0014} _{-0.0015}	V 390m4 UT 2020-08-18 (I) MSU UT 2021-10-24 (Kepler) 2.42 ^{+0.59} _{-0.59} 0.139 ^{+0.044} _{-0.046}	OPM UT 2020-10-29 (z')	CALOU UT 2020-11-23 (B)
F_0	1.00067 ± 0.00021	0.99986 ± 0.00064	0.9959 ± 0.0012	0.99915 ^{+0.00027} _{-0.00028}
C_0	1.00037 ± 0.00033	0.0004 ± 0.0011	0.0010 ± 0.0022	—
C_0	0.00116 ± 0.00078	0.00064 ± 0.00041	—	—
M_0	—	—	—	0.00160 ± 0.00054
TOI-2497				
Wavelength Parameters:				
u_1	0.156 ^{+0.035} _{-0.034}	—	—	—
u_2	0.327 ± 0.036	—	—	—
Telescope Parameters:				
γ_{rel}	CHIRON MINERVAT6 43 ± 24	MINERVAT3 TRES 5586 ⁺⁸³ ₋₇₉	MINERVAT4 MINERVAT5	MINERVAT5
σ_J	—342 ⁺²⁷ ₋₂₇	210 ⁺⁸³ ₋₆₉	56050 ⁺¹¹⁰ ₋₁₀₀	56280 ± 100
σ_J^2	78 ⁺³⁰ ₋₂₇	83 ⁺²⁸ ₋₂₈	251 ⁺²¹⁰ ₋₉₉	80 ⁺²¹⁰ ₋₈₁
σ_J^2	6100 ⁺⁵⁵⁰⁰ ₋₆₃₀₀	44000 ⁺⁴²⁰⁰⁰ ₋₂₄₀₀₀	63000 ⁺⁷⁵⁰⁰⁰ ₋₄₀₀₀₀	7000 ⁺⁷⁶⁰⁰⁰ ₋₃₅₀₀₀
Transit Parameters:				
σ^2	TESS S6 0.015 ^{+0.00013} _{-0.00010}	TESS S33 0.0018 ± 0.016	—	—
F_0	1.000031 ^{+0.000033} _{-0.000033}	1.000258 ± 0.000019	—	—

support from the European Research Council under the Horizon 2020 Framework Program via the ERC Advanced Grant Origins 83 24 28. JVS acknowledges funding from the European Research Council (ERC) under the European Union’s Horizon 2020 research and innovation programme (project Four Aces; grant agreement No. 724427). PR acknowledges support from NSF grant No. 1952545. RB and AJ acknowledges support from FONDECYT Projects 11200751 and 1210718 and from the CORFO project N°14ENI2-26865. AJ, RB and MH acknowledge support from project IC120009 ‘Millennium Institute of Astrophysics (MAS)’ of the Millennium Science Initiative, Chilean Ministry of Economy. The Pennsylvania State University Eberly College of Science. The Center for Exoplanets and Habitable Worlds is supported by the Pennsylvania State University, the Eberly College of Science, and the Pennsylvania Space Grant Consortium. KKM gratefully acknowledges support from the New York Community Trust’s Fund for Astrophysical Research. LG and AG are supported by NASA Massachusetts Space Grant Fellowships. EWG, ME, and PC acknowledge support by Deutsche Forschungsgemeinschaft (DFG) grant HA 3279/12-1 within the DFG Schwerpunkt SPP1992, Exploring the Diversity of Extrasolar Planets. BSG was partially supported by the Thomas Jefferson Chair for Space Exploration at the Ohio State University. CD acknowledges support from the Hellman Fellows Fund and NASA XRP via grant 80NSSC20K0250. BSS, MVG, and AAB acknowledge the support of Ministry of Science and Higher Education of the Russian Federation under the grant 075-15-2020-780 (N13.1902.21.0039). BA is supported by Australian Research Council Discovery Grant DP180100972. TRB acknowledges support from the Australian Research Council (DP210103119). TRB acknowledges support from the Australian Research Council (DP210103119 and FL220100117).

The authors thank the CHIRON team members, including Todd Henry, Leonardo Paredes, Hodari James, Azmain Nisak, Rodrigo Hinojosa, Roberto Aviles, Wei-Chun Jao, and CTIO staffs, for their work in acquiring RVs with CHIRON at CTIO. This research has made use of SAO/NASA’s Astrophysics Data System Bibliographic Services. This research has made use of the SIMBAD database, operated at CDS, Strasbourg, France. This work has made use of data from the European Space Agency (ESA) mission *Gaia* (<https://www.cosmos.esa.int/gaia>), processed by the *Gaia* Data Processing and Analysis Consortium (DPAC, <https://www.cosmos.esa.int/web/gaia/dpac/consortium>). Funding for the DPAC has been provided by national institutions, in particular the institutions participating in the *Gaia* Multilateral Agreement. This work makes use of observations from the LCO network. Based in part on observations obtained at the Southern Astrophysical Research (SOAR) telescope, which is a joint project of the Ministério da Ciência, Tecnologia e Inovações (MCTI/LNA) do Brasil, the US National Science Foundation’s NOIRLab, the University of North Carolina at Chapel Hill (UNC), and Michigan State University (MSU).

Funding for the *TESS* mission is provided by NASA’s Science Mission directorate. The authors acknowledge the use of public *TESS* Alert data from pipelines at the *TESS* Science Office and at the *TESS* Science Processing Operations Center. This research has made use of the NASA Exoplanet Archive and the Exoplanet Follow-up Observation Program website, which are operated by the California Institute of Technology, under contract with the National Aeronautics and Space Administration under the Exoplanet Exploration Program. This paper includes data collected by the *TESS* mission, which are publicly available from the Mikulski Archive for Space Telescopes (MAST). This paper includes observations obtained under Gemini program GN-2018B-LP-101. Resources supporting this work were provided by the NASA High-End Computing (HEC) Program

through the NASA Advanced Supercomputing (NAS) Division at Ames Research Center for the production of the SPOC data products. This publication makes use of The Data and Analysis Center for Exoplanets (DACE), which is a facility based at the University of Geneva (CH) dedicated to extrasolar planets data visualisation, exchange and analysis. DACE is a platform of the Swiss National Centre of Competence in Research (NCCR) PlanetS, federating the Swiss expertise in Exoplanet research. The DACE platform is available at <https://dace.unige.ch>.

Some of the data presented herein were obtained at the W. M. Keck Observatory, which is operated as a scientific partnership among the California Institute of Technology, the University of California and the National Aeronautics and Space Administration. The Observatory was made possible by the generous financial support of the W. M. Keck Foundation. The authors wish to recognize and acknowledge the very significant cultural role and reverence that the summit of Mauna Kea has always had within the indigenous Hawaiian community. We are most fortunate to have the opportunity to conduct observations from this mountain.

MINERVA-Australis is supported by Australian Research Council LIEF Grant LE160100001 (Discovery Grant DP180100972 and DP220100365) Mount Cuba Astronomical Foundation, and institutional partners University of Southern Queensland, UNSW Sydney, MIT, Nanjing University, George Mason University, University of Louisville, University of California Riverside, University of Florida, and The University of Texas at Austin. The authors respectfully acknowledge the traditional custodians of all lands throughout Australia and recognize their continued cultural and spiritual connection to the land, waterways, cosmos, and community. The authors pay our deepest respects to all Elders, ancestors and descendants of the Giabal, Jarowair, and Kambuwal nations, upon whose lands the MINERVA-Australis facility at Mt Kent is situated.

Data presented herein were obtained at the MINERVA-Australis from telescope time allocated under the NN-EXPLORE program with support from the National Aeronautics and Space Administration.

MINERVA-North is a collaboration among the Harvard-Smithsonian Center for Astrophysics, The Pennsylvania State University, the University of Montana, the University of Southern Queensland, University of Pennsylvania, and George Mason University. It is made possible by generous contributions from its collaborating institutions and Mt. Cuba Astronomical Foundation, The David & Lucile Packard Foundation, National Aeronautics and Space Administration (EPSCOR grant NNX13AM97A, XRP 80NSSC22K0233), the Australian Research Council (LIEF grant LE140100050), and the National Science Foundation (grants 1516242, 1608203, and 2007811).

This article is based on observations made with the MuSCAT2 instrument, developed by ABC, at Telescopio Carlos Sánchez operated on the island of Tenerife by the IAC in the Spanish Observatorio del Teide. This work is partly financed by the Spanish Ministry of Economics and Competitiveness through grants PGC2018-098153-B-C31. The work of VK was supported by the Ministry of science and higher education of the Russian Federation, topic FEUZ-2020-0038.

This work is partly supported by JSPS KAKENHI Grant Number JP18H05439, JST CREST Grant Number JPMJCR1761. This article is based on observations made with the MuSCAT2 instrument, developed by ABC, at Telescopio Carlos Sánchez operated on the island of Tenerife by the IAC in the Spanish Observatorio del Teide.

The Center for Exoplanets and Habitable Worlds and the Penn State Extraterrestrial Intelligence Center are supported by Penn State and the Eberly College of Science.

This paper was partially based on observations obtained at the OWL-Net system, which is operated by the Korea Astronomy and Space Science Institute (KASI).

DATA AVAILABILITY

The *TESS* observations used in this paper (see Section 2.1) and are shown in Fig. 1 are publicly available on the MAST¹¹ archive. The photometric transit follow up observations from the SG1 working groups in TFOP (underlying data for Figs 3 and 4) are publicly available on Exofop at <https://exofop.ipac.caltech.edu/tess/>, along with the the AO and SPECKLE contrast curves and images discussed in §2.6. The RV data (sample shown in Table 3) underlying this article (shown in Fig. 5) are available within the article and in its online supplementary material.

Software Used: EXOFASTv2 (Eastman et al. 2013; Eastman et al. 2019), AstroImageJ (Collins et al. 2017), TAPIR (Jensen 2013), QLP Pipeline (Huang et al. 2020)

Facilities: *TESS*, FLWO 1.5m (Tillinghast Reflector Echelle Spectrograph), 4.1-m Southern Astrophysical Research (SOAR), LCO 0.4m, LCO 1.0m, 2.2m telescope La Silla (Fiber-fed Extended Range Optical Spectrograph), KECK (NIRC2), PALOMAR (PHARO), KELT, WASP, CTIO 1.5m (CHIRON), MINERVA-North, MINERVA-Australis, GEMINI (NIRI), CMO 2.5m (SPP)

REFERENCES

- Adams F. C., Laughlin G., 2006, *ApJ*, 649, 1004
 Addison B. et al., 2019, *PASP*, 131, 115003
 Addison B. C. et al., 2021, *MNRAS*, 502, 3704
 Almenara J. M. et al., 2015, *A&A*, 575, A71
 Auvergne M. et al., 2009, *A&A*, 506, 411
 Bakos G. Á. et al., 2013, *PASP*, 125, 154
 Barclay T., Pepper J., Quintana E. V., 2018, *ApJS*, 239, 2
 Barros S. C. C., Demangeon O., Deleuil M., 2016, *A&A*, 594, A100
 Borucki W. J. et al., 2010, *Science*, 327, 977 20056856
 Boyajian T. S. et al., 2012, *ApJ*, 757, 112
 Bradley L. et al., 2019, preprint (astro/photutils: v0.7.1)
 Brahm R. et al., 2020, *AJ*, 160, 235
 Brasseur C. E., Phillip C., Fleming S. W., Mullally S. E., White R. L., 2019, *Astrocute: Tools for creating cutouts of TESS images*. Astrophysics Source Code Library, preprint (ascl:1905.007)
 Brown T. M. et al., 2013, *PASP*, 125, 1031
 Buchhave L. A. et al., 2010, *ApJ*, 720, 1118
 Buchhave L. A. et al., 2012, *Nature*, 486, 375 22722196
 Burdanov A. Y., Krushinsky V. V., Popov A. A., 2014, *Astrophys. Bull.*, 69, 368
 Caldwell D. A. et al., 2020, *Res. Notes Am. Astron. Soc.*, 4, 201
 Cale B. et al., 2019, *AJ*, 158, 170
 Carmichael T. W. et al., 2021, *AJ*, 161, 97
 Castelli F., Hubrig S., 2004, *A&A*, 425, 263
 Choi J., Dotter A., Conroy C., Cantiello M., Paxton B., Johnson B. D., 2016, *ApJ*, 823, 102
 Ciardi D. R., Beichman C. A., Horch E. P., Howell S. B., 2015, *ApJ*, 805, 16
 Collier Cameron A. et al., 2007, *MNRAS*, 380, 1230
 Collins K. A., Kielkopf J. F., Stassun K. G., Hessman F. V., 2017, *AJ*, 153, 77
 Crossfield I. J. M. et al., 2016, *ApJS*, 226, 7
 Cumming A., Butler R. P., Marcy G. W., Vogt S. S., Wright J. T., Fischer D. A., 2008, *PASP*, 120, 531
 Cutri R. M. et al., 2003, *AJ*, 131, 1163
 Cutri R. M. et al., 2010, *AJ*, 140, 1868
 Czesla S., Schröter S., Schneider C. P., Huber K. F., Pfeifer F., Andreasen D. T., Zechmeister M., 2019, PyA: Python astronomy-related packages. Astrophysics Source Code Library, preprint (ascl:1906.010)
 Dawson R. I., Fabrycky D. C., 2010, *ApJ*, 722, 937
 Dawson R. I., Johnson J. A., 2018, *Annu. Rev. Astron. Astrophys.*, 56, 175
 Dekany R. et al., 2013, *ApJ*, 776, 130
 Dotter A., 2016, *ApJS*, 222, 8
 Eastman J., Gaudi B. S., Agol E., 2013, *PASP*, 125, 83
 Eastman J. D. et al., 2019, preprint (arXiv:1907.09480)
 Edwards B. et al., 2021, *MNRAS*, 504, 5671
 Fűrész G., 2008, PhD thesis, University of Szeged, Hungary
 Fortney J. J., Dawson R. I., Komacek T. D., 2021, *J. Geophys. Res. (Planets)*, 126, e06629
 Fressin F. et al., 2013, *ApJ*, 766, 81
 Furlan E. et al., 2017, *AJ*, 153, 71
 Gaia Collaboration et al., 2016, *A&A*, 595, A2
 Gaia Collaboration et al., 2018, *A&A*, 616, A1
 Gaia Collaboration et al., 2021, *A&A*, 649, A1
 Gaudi B. S., Seager S., Mallen-Ornelas G., 2005, *ApJ*, 623, 472
 Gavel D. et al., 2014, in Marchetti E., Close L. M., Vran J.-Peds, Soc. Photo-Optical Instrum. Eng. (SPIE) Conf. Ser. Vol. 9148, Adaptive Optics Syst. IV. p. 914805, preprint (arXiv:1407.8207),
 Grunblatt S. K. et al., 2016, *AJ*, 152, 185
 Grunblatt S. K. et al., 2022, *AJ*, 163, 120
 Guerrero N. M. et al., 2021, *ApJS*, 254, 39
 Hardegree-Ullman K. K., Zink J. K., Christiansen J. L., Dressing C. D., Ciardi D. R., Schlieder J. E., 2020, *ApJS*, 247, 28
 Hartman J. D., Bakos G. Á., 2016, *Astron. Comput.*, 17, 1
 Hayward T. L., Brandl B., Pirger B., Blacken C., Gull G. E., Schoenwald J., Houck J. R., 2001, *PASP*, 113, 105
 Henderson C. B., Stassun K. G., 2012, *ApJ*, 747, 51
 Howell S. B. et al., 2014, *PASP*, 126, 398
 Huang C. X. et al., 2020, *Res. Notes Am. Astron. Soc.*, 4, 206
 Ikwut-Ukwa M. et al., 2020, *AJ*, 160, 209
 Ikwut-Ukwa M. et al., 2022, *AJ*, 163, 9
 Jenkins J. M., 2002, *ApJ*, 575, 493
 Jenkins J. M. et al., 2016, in Software and Cyberinfrastructure for Astronomy IV. p. 99133E,
 Jensen E., 2013, Tapir: A web interface for transit/eclipse observability, Astrophysics Source Code Library preprint (ascl:1306.007)
 Johnson M. C., Cochran W. D., Albrecht S., Dodson-Robinson S. E., Winn J. N., Gullikson K., 2014, *ApJ*, 790, 30
 Jones M. I. et al., 2019, *A&A*, 625, A16
 Kane S. R. et al., 2021, *PASP*, 133, 014402
 Knudstrup E. et al., 2022, *A&A*, 667, A22
 Komacek T. D., Thorngren D. P., Lopez E. D., Ginzburg S., 2020, *ApJ*, 893, 36
 Kovács G., Bakos G., Noyes R. W., 2005, *MNRAS*, 356, 557
 Kuhn R. B. et al., 2016, *MNRAS*, 459, 4281
 Kupke R. et al., 2012, in Ellerbroek B. L., Marchetti E., Véran J.-Peds, Society of Photo-Optical Instrumentation Engineers (SPIE) Conference Series Vol. 8447, Adaptive Optics Systems III. p. 84473G,
 Lindgren L. et al., 2018, *A&A*, 616, A2
 Lomb N. R., 1976, *Ap&SS*, 39, 447
 Lopez E. D., Fortney J. J., 2016, *ApJ*, 818, 4
 Masuda K., Winn J. N., 2017, *AJ*, 153, 187
 Maxted P. F. L. et al., 2011, *PASP*, 123, 547
 Mayo A. W. et al., 2018, *AJ*, 155, 136
 McGurk R. et al., 2014, in Marchetti E., Close L. M., Vran J.-Peds, Society of Photo-Optical Instrumentation Engineers (SPIE) Conference Series Vol. 9148, Adaptive Optics Systems IV. p. 91483A, preprint (arXiv:1407.8205)
 McLaughlin D. B., 1924, 22 *ApJ*, 60
 Miller G. R. M. et al., 2010, *A&A*, 523, A52
 Moe M., Kratter K. M., 2021, *MNRAS*, 507, 3593
 Mugrauer M., Michel K.-U., 2020, *Astron. Nachr.*, 341, 996
 Mugrauer M., Michel K.-U., 2021, *Astron. Nachr.*, 342, 840
 Narita N. et al., 2019, *J. Astron. Telesc., Instrum. Syst.*, 5, 015001

¹¹<https://mast.stsci.edu/>

- Nelson B. E., Ford E. B., Rasio F. A., 2017, *AJ*, 154, 106
- Nielsen L. D. et al., 2019, *A&A*, 623, A100
- Oelkers R. J. et al., 2018, *AJ*, 155, 39
- Paredes L. A., Henry T. J., Quinn S. N., Gies D. R., Hinojosa-Goni R., James H.-S., Jao W.-C., White R. J., 2021, *AJ*, 162, 176
- Parviainen H. et al., 2019, *A&A*, 630, A89
- Paxton B., Bildsten L., Dotter A., Herwig F., Lesaffre P., Timmes F., 2011, *ApJS*, 192, 3
- Paxton B. et al., 2013, *ApJS*, 208, 4
- Paxton B. et al., 2015, *ApJS*, 220, 15
- Pecaut M. J., Mamajek E. E., 2013a, *ApJS*, 208, 9
- Pecaut M. J., Mamajek E. E., 2013b, *ApJS*, 208, 9
- Pepper J. et al., 2007, *PASP*, 119, 923
- Pepper J., Kuhn R. B., Siverd R., James D., Stassun K., 2012, *PASP*, 124, 230
- Pepper J., Stassun K. G., Gaudi B. S., 2018, *KELT: The Kilodegree Extremely Little Telescope, a Survey for Exoplanets Transiting Bright, Hot Stars*. Springer International Publishing, 128
- Petigura E. A. et al., 2018, *AJ*, 155, 89
- Pollacco D. L. et al., 2006, *PASP*, 118, 1407
- Quinn S. N. et al., 2012, *ApJ*, 756, L33
- Rasio F. A., Ford E. B., 1996, *Science*, 274, 954 8875930
- Ricker G. R. et al., 2015, *J. Astron. Teles. Instrum. Syst.*, 1, 014003
- Rodriguez J. E. et al., 2019, *AJ*, 157, 191
- Rodriguez J. E. et al., 2021, *AJ*, 161, 194
- Rossiter R. A., 1924, 15 *ApJ*, 60
- Safonov B. S., Lysenko P. A., Dodin A. V., 2017, *Astron. Lett.*, 43, 344
- Savel A. B., Dressing C. D., Hirsch L. A., Ciardi D. R., Fleming J. P. C., Giacalone S. A., Mayo A. W., Christiansen J. L., 2020, *AJ*, 160, 287
- Scargle J. D., 1982, *ApJ*, 263, 835
- Schlafly E. F., Finkbeiner D. P., 2011, *ApJ*, 737, 103
- Schlegel D. J., Finkbeiner D. P., Davis M., 1998, *ApJ*, 500, 525
- Shallue C. J., Vanderburg A., 2018, *AJ*, 155, 94
- Siverd R. J. et al., 2012, *ApJ*, 761, 123
- Smith J. C. et al., 2012, *PASP*, 124, 1000
- Stassun K. G., Torres G., 2016, *AJ*, 152, 180
- Stassun K. G., Mathieu R. D., Mazeh T., Vrba F. J., 1999, *AJ*, 117, 2941
- Stassun K. G. et al., 2018, *AJ*, 156, 102
- Stevens D. J. et al., 2017, *AJ*, 153, 178
- Stumpe M. C., Smith J. C., Catanzarite J. H., Van Cleve J. E., Jenkins J. M., Twicken J. D., Girouard F. R., 2014, *PASP*, 126, 100
- Sullivan P. W. et al., 2015, *ApJ*, 809, 77
- Swift J. J. et al., 2015, *J. Astron. Telesc. Instrum. Syst.*, 1, 027002
- Tinetti G. et al., 2016, in MacEwen H. A., Fazio G. G., Lystrup M., Batalha N., Siegler N., Tong E. C. eds, *Soc. Photo-Optical Instrum. Eng. (SPIE) Conference Series Vol. 9904, Space Telescopes and Instrumentation 2016: Optical, Infrared, and Millimeter Wave*. p. 99041X,
- Tokovinin A., 2018, *PASP*, 130, 035002
- Tokovinin A., Fischer D. A., Bonati M., Giguere M. J., Moore P., Schwab C., Spronck J. F. P., Szymkowiak A., 2013, *PASP*, 125, 1336
- Torres G. et al., 2007, *ApJ*, 666, L121
- VanderPlas J. T., 2018, *ApJS*, 236, 16
- Vanderburg A., Johnson J. A., 2014, *PASP*, 126, 948
- Vanderburg A. et al., 2016, *ApJS*, 222, 14
- Vanderburg A. et al., 2019, *ApJ*, 881, L19
- Wilson M. L. et al., 2019, preprint (arXiv:1904.09991)
- Wright J. T., Marcy G. W., Howard A. W., Johnson J. A., Morton T. D., Fischer D. A., 2012, *ApJ*, 753, 160
- Wu Y., Lithwick Y., 2011, *ApJ*, 735, 109
- Yee S. W., Winn J. N., Hartman J. D., 2021, *AJ*, 162, 240
- Zhou G. et al., 2016, *AJ*, 152, 136
- Zhou G. et al., 2019, *AJ*, 158, 141
- Zhou G. et al., 2021, *AJ*, 161, 2
- Ziegler C. et al., 2018, *AJ*, 155, 161
- Ziegler C., Tokovinin A., Briceño C., Mang J., Law N., Mann A. W., 2020, *AJ*, 159, 19
- Zink J. K. et al., 2019, *Res. Notes Am. Astron. Soc.*, 3, 43
- Zink J. K. et al., 2021, *AJ*, 162, 259

SUPPORTING INFORMATION

Supplementary data are available at [MNRAS](https://www.mnras.org/online) online.

Please note: Oxford University Press is not responsible for the content or functionality of any supporting materials supplied by the authors. Any queries (other than missing material) should be directed to the corresponding author for the article.

¹Center for Data Intensive and Time Domain Astronomy, Department of Physics and Astronomy, Michigan State University, East Lansing, MI 48824, USA

²Center for Astrophysics | Harvard & Smithsonian, 60 Garden St, Cambridge, MA 02138, USA

³Department of Physics and Kavli Institute for Astrophysics and Space Research, Massachusetts Institute of Technology, Cambridge, MA 02139, USA

⁴Centre for Astrophysics, University of Southern Queensland, West Street, Toowoomba, QLD 4350, Australia

⁵Caltech IPAC – NASA Exoplanet Science Institute 1200 E. California Ave, Pasadena, CA 91125, USA

⁶Department of Physical Sciences, Kutztown University, Kutztown, PA 19530, USA

⁷George P. and Cynthia Woods Mitchell Institute for Fundamental Physics and Astronomy, Texas A&M University, College Station, TX 77843 USA

⁸Charles R. & Judith G. Munneryn Astronomical Laboratory, Department of Physics & Astronomy, Texas A&M University, College Station, TX 77843, USA

⁹Center for Gravitational Wave Astronomy, The University of Texas Rio Grande Valley, Brownsville, TX 78520, USA

¹⁰Department of Astronomy and Astrophysics, University of California, Santa Cruz, CA 95064, USA

¹¹Department of Astronomy, The Ohio State University, 140 West 18th Avenue, Columbus, OH 43210, USA

¹²Astrophysics Group, Keele University, Staffordshire ST5 5BG, UK

¹³European Southern Observatory, Alonso de Córdova 3107, Vitacura, Casilla 19001, Santiago, Chile

¹⁴Facultad de Ingeniería y Ciencias, Universidad Adolfo Ibáñez, Av. Diagonal las Torres 2640, Peñalolén, Santiago 7941169, Chile

¹⁵Millennium Institute for Astrophysics, Chile

¹⁶Data Observatory Foundation, Chile

¹⁷Kotizarovci Observatory, Sarsoni 90, Viskovo 51216, Croatia

¹⁸Department of Physics and Astronomy, University of Louisville, Louisville, KY 40292, USA

¹⁹Observatori de Ca l'Ou

²⁰Villa '39 Observatory, Landers, CA 92285, USA

²¹Evans, El Sauce Observatory, Coquimbo Province, Chile

²²Department of Physics and Astronomy, Brigham Young University, Provo, UT 84602, USA

²³Department of Astronomy, Wellesley College, Wellesley, MA 02481, USA

²⁴Ural Federal University, Ekaterinburg, Russia, ul. Mira d. 19, Yekaterinburg 620002, Russia

²⁵Oukaimeden Observatory, High Energy Physics and Astrophysics Laboratory, Cadi Ayyad University, Marrakech 40000, Morocco

²⁶Astrobiology Research Unit, Université de Liège, 19C Allée du 6 Août, Liège 4000, Belgium

²⁷Sternberg Astronomical Institute, M.V. Lomonosov Moscow State University, 13, Universitetskij pr., Moscow 119234, Russia

²⁸Department of Astronomy & Astrophysics, The Pennsylvania State University, 525 Davey Lab, University Park, PA 16802, USA

²⁹Center for Exoplanets and Habitable Worlds, The Pennsylvania State University, 525 Davey Lab, University Park, PA 16802, USA

³⁰American Association of Variable Star Observers 185 Alewife Brook Parkway, Suite 410 Cambridge, MA 02138 USA

- ³¹Department of Astronomy, University of California Berkeley, Berkeley, CA 94720-3411, USA
- ³²Department of Physics, Engineering and Astronomy, Stephen F. Austin State University, TX 75962, USA
- ³³Observatori Astronòmic Albanyà, Camí de Bassegoda S/N, Albanyà 17733, Girona, Spain
- ³⁴Citizen Scientist
- ³⁵Instituto de Astrofísica de Canarias (IAC), La Laguna E-38205, Tenerife, Spain
- ³⁶Departamento de Astrofísica, Universidad de La Laguna (ULL), La Laguna E-38206, Tenerife, Spain
- ³⁷Waffelow Creek Observatory
- ³⁸Department of Earth, Atmospheric and Planetary Sciences, Massachusetts Institute of Technology, Cambridge, MA 02139, USA
- ³⁹Department of Aeronautics and Astronautics, MIT, 77 Massachusetts Avenue, Cambridge, MA 02139, USA
- ⁴⁰Department of Astrophysical Sciences, Princeton University, 4 Ivy Lane, Princeton, NJ 08544, USA
- ⁴¹NASA Ames Research Center, Moffett Field, CA 94035, USA
- ⁴²Swinburne University of Technology, Centre for Astrophysics and Supercomputing, John Street, Hawthorn, VIC 3122, Australia
- ⁴³George Mason University, 4400 University Drive MS 3F3, Fairfax, VA 22030, USA
- ⁴⁴Department of Physics, University of Warwick, Gibbet Hill Road, Coventry CV4 7AL, UK
- ⁴⁵Department of Astronomy, University of Wisconsin-Madison, Madison, WI 53706, USA
- ⁴⁶School of Physics, Sydney Institute for Astronomy (SfA), The University of Sydney, NSW 2006, Australia
- ⁴⁷The University of Pennsylvania, Department of Physics and Astronomy, Philadelphia, PA 19104, USA
- ⁴⁸Department of Astronomy, The University of Texas at Austin, Austin, TX 78712, USA
- ⁴⁹Department of Physics and Astronomy, University of Montana, 32 Campus Drive, No. 1080, Missoula, MT 59812 USA
- ⁵⁰Cerro Tololo Inter-American Observatory, Casilla 603, La Serena, Chile
- ⁵¹Department of Physics and Astronomy, University of Utah, 115 South 1400 East, Salt Lake City, UT 84112, USA
- ⁵²Fundamental and Applied Physics Laboratory, Physics Department, Polydisciplinary Faculty of Safi, Cadi Ayyad University, Marrakesh 40000, Morocco
- ⁵³Department of Physics and Astronomy, Vanderbilt University, Nashville, TN 37235, USA
- ⁵⁴Komaba Institute for Science, The University of Tokyo, 3-8-1 Komaba, Meguro, Tokyo 153-8902, Japan
- ⁵⁵Department of Astronomy, Tsinghua University, Beijing 100084, China
- ⁵⁶Max-Planck-Institut für Astronomie, Königstuhl 17, Heidelberg 69117, Germany
- ⁵⁷ASTRAVEO, LLC, PO Box 1668, Gloucester, MA 01931, USA
- ⁵⁸Department of Earth and Planetary Sciences, University of California, Riverside, CA 92521, USA
- ⁵⁹Korea Astronomy and Space Science Institute, 776 Daedeok-daero, Yuseong-gu, Daejeon 34055, Republic of Korea
- ⁶⁰Thomas Jefferson High School, 6560 Braddock Rd, Alexandria, VA 22312, USA
- ⁶¹South African Astronomical Observatory, PO Box 9, Observatory, Cape Town 7935, South Africa
- ⁶²Southern African Large Telescope, PO Box 9, Observatory, Cape Town 7935, South Africa
- ⁶³Department of Physics and Astronomy, University of North Carolina at Chapel Hill, Chapel Hill, NC 27599, USA
- ⁶⁴Maurly Lewin Astronomical Observatory, Glendora, CA 91741, USA
- ⁶⁵School of Astronomy and Space Science, Key Laboratory of Modern Astronomy and Astrophysics in Ministry of Education, Nanjing University, Nanjing 210046, Jiangsu, China
- ⁶⁶Astrobiology Center, 2-21-1 Osawa, Mitaka, Tokyo 181-8588, Japan
- ⁶⁷Physikalisches Institut, University of Bern, Gesellschaftsstrasse 6, Bern 3012, Switzerland
- ⁶⁸Department of Physics, Lehigh University, 16 Memorial Drive East, Bethlehem, PA 18015, USA
- ⁶⁹Departamento de Matemática y Física Aplicadas, Facultad de Ingeniería, Universidad Católica de la Santísima Concepción, Alonso de Rivera 2850, Concepción, Chile
- ⁷⁰Department of Astronomy, University of Maryland, College Park, College Park, MD 20742, USA
- ⁷¹Patashnick Voorheesville Observatory, Voorheesville, NY 12186, USA
- ⁷²Gemini Observatory/NSF's NOIRLab, 670 N. A'ohoku Place, Hilo, HI 96720, USA
- ⁷³Department of Physics, Fisk University, 1000 17th Avenue North, Nashville, TN 37208, USA
- ⁷⁴University of Minnesota Duluth, Duluth, MN 55812, USA
- ⁷⁵Instituto de Astrofísica e Ciências do Espaço, CAUP, Universidade do Porto, Rua das Estrelas, Porto 4150-762, Portugal
- ⁷⁶Departamento de física, e Astronomia, Faculdade de Ciências, Universidade do Porto, Rua Campo Alegre 4169-007, Porto, Portugal
- ⁷⁷Exoplanetary Science at UNSW, School of Physics, UNSW Sydney, NSW 2052, Australia
- ⁷⁸Centre for Exoplanets and Habitability, University of Warwick, Gibbet Hill Road, Coventry CV4 7AL, UK
- ⁷⁹Penn State Extraterrestrial Intelligence Center, 525 Davey Laboratory, The Pennsylvania State University, University Park, PA, 16802, USA
- ⁸⁰Shanghai Astronomical Observatory, Chinese Academy of Sciences, Shanghai 200030, China

This paper has been typeset from a $\text{\TeX}/\text{\LaTeX}$ file prepared by the author.